



**Politecnico  
di Torino**

**POLITECNICO DI TORINO**

Facoltà di Ingegneria

Corso di Laurea Magistrale in Ingegneria Energetica e Nucleare

A.a. 2022/2023

Tesi di Laurea Magistrale

**Mid-fidelity Model with CFD Damping Correction  
for Floating Offshore Wind Turbine  
Productivity Evaluation**

Relatore:

Prof. Giovanni Bracco

Co-relatore:

Oronzo Dell'Edera

Candidato:

Lorenzo Dutto

Ottobre 2023



# Index

<b>Acronyms and abbreviations</b> .....	<b>2</b>
<b>Abstract</b> .....	<b>4</b>
<b>Introduction</b> .....	<b>6</b>
<b>Literature review</b> .....	<b>10</b>
The modelling of a FOWT and the evaluation of its characteristics .....	11
Examples of FOWT modelling .....	13
Verification and validation of numerical models .....	15
<b>Free decay simulations</b> .....	<b>19</b>
VoluturnUS-S platform geometry, mesh generation and boundary conditions .....	19
Pitch free decay .....	21
Mesh generation and boundary conditions .....	23
Time step .....	27
Volume of Fluid (VOF) .....	28
Turbulence model, wall treatment, and $Y^+$ .....	28
Dynamic Fluid Body Interaction (DFBI) .....	30
Space and time discretization convergence studies and uncertainty analysis .....	30
Comparison between different simulation setups .....	41
Heave free decay .....	47
Simulation setup .....	48
Space and time discretization convergence studies and uncertainty analysis .....	50
<b>Results and post-processing</b> .....	<b>55</b>
<b>Case study productivity estimation</b> .....	<b>60</b>
Environmental conditions selection .....	60
Productivity estimation and comparison .....	62
<b>Conclusion</b> .....	<b>65</b>
<b>Bibliography</b> .....	<b>66</b>

# Acronyms and abbreviations

**ALM** – Actuator Line Method

**AMI** – Arbitrary Mesh Interface

**AMR** – Adaptive Mesh Refinement

**BEM** – Blade Element Momentum (theory)

**CFD** – Computational Fluid Dynamics

**DFBI** – Dynamic Fluid-Body Interaction (approach)

**DLC** – Design Load Case

**DNS** – Direct Numerical Simulation

**DOF** – Degree of Freedom

**ECMWF** – European Center for Medium-range Weather Forecasts

**FOWT** – Floating Offshore Wind Turbine

**FVM** – Finite Volume Method

**GCI** – Grid Convergence Index

**IEA** – International Energy Agency

**IRENA** – International Renewable Energy Agency

**k- $\omega$  SST** – k- $\omega$  Shear Stress Transport (model)

**LES** – Large Eddy Simulation

**MARIN** – Maritime Research Institute Netherlands

**MBS** – Multibody System

**MORE** – Marine Offshore Renewable Energy (Laboratory)

**NREL** – National Renewable Energy Laboratory

**NSE** – Navier-Stokes Equations

**OC3** - Offshore Code Comparison Collaboration (initiative)

**OC4** - Offshore Code Comparison Collaboration Continuation (initiative)

**OC5** - Offshore Code Comparison Collaboration, Continued, with Correlation (initiative)

**PDE** – Partial Differential Equation

**RANS** – Reynolds-Averaged Navier-Stokes

**RE** – Richardson Extrapolation (method)

**RES** – Renewable Energy Sources

**SRH** – Scale Resolving Hybrid (turbulence model)

**SWL** – Still Water Level

**TLP** – Tension Leg Platform

**V&V** – Verification and Validation

**VOF** – Volume of Fluid (method)

**WD** – Wall Distance (model)

# Abstract

Renewable Energy Sources play a central role in the fight against climate change, as they represent one of the most important paradigms on which a renovated and sustainable society should be built. Among them, offshore wind energy is growing in popularity, as it represents a great opportunity to efficiently harness the vast potential of wind energy at sea. In particular, floating offshore wind turbines (FOWT) are the only viable solution at higher bathymetry and thus they could open up the possibility for a much wider installation worldwide. FOWTs are stabilized thanks to the structure on which they are built, moored to the seabed. Usually, they are divided in three categories: mass stabilized structures, buoyancy stabilized structures, and tension leg platforms. Each solution has different advantages and disadvantages, mostly linked to their performance, construction methods and cost. As researchers and the industry aim at installing bigger and more efficient turbines, there is a strong commitment to the development of innovative solutions to support floating offshore wind turbines. However, experts have to deal with multiple interconnected problems in the design of these solutions, such as the prediction of their interaction with wave and wind loads or the design of an effective control system.

The focus of this thesis is the accurate evaluation of the energy produced by a floating offshore wind turbine. In particular, this work is centered around the UMaine VoltturnUS-S Reference Platform, which is a semi-submersible floating platform specifically designed to work with the IEA 15MW reference turbine. This turbine is currently the largest available reference device, and it is an excellent example of the trend to go towards bigger and more powerful turbines. In order to estimate the productivity of the turbine, it is necessary to correctly model the interaction between the structure and the environment in which it should be installed. As it is a body with a complex geometry, an accurate description of its dynamic properties could lead to an improvement in the prediction of its performance. Therefore, a CFD simulation of the semi-submersible structure is performed within Star-CCM+, posing particular attention on the free decay motion for the pitch and heave motions. Post-processing techniques are then used in order to extrapolate first and second order damping coefficients. These results, obtained from a high accuracy model, are then used in lower-accuracy models to check their effect on the prediction of the productivity of a turbine under a set of reference conditions.

In this work, an accurate analysis of the CFD model is performed, in order to optimize the simulation in terms of computational time and accuracy, while testing the effect of different mesh parameters, simulation strategies and numerical models. From the result of this process, a set of

accurate descriptors for the body motion is obtained. The main goal is to assess the benefits that a preliminary CFD analysis can bring to a lower-accuracy simulation of the turbine performance, in order to improve the overall quality of future works on the subject.

# Introduction

As the climate crisis poses serious threats to our society, the need for an energy transition is stronger than ever. Renewable Energy Sources (RES) are unanimously recognized as a key asset for a renovated and sustainable society. Generally associated with the reduction of greenhouse gases emissions, they represent a paradigm change from multiple point of views, most importantly a shift from a centralized energy system to a distributed one. While there are still some unsolved problems, e.g. the need for critical raw materials, recent events are showing the many benefits that renewables can offer. For example, as reported by the International Energy Agency (IEA) [1], the global energy crisis caused by Russia's invasion of Ukraine pushed governments to improve their renewable energy policies to address the energy security problem, while increasing fossil fuel prices are benefitting solar and wind energy competitiveness. Not only RES installation and innovation are growing, but they are accelerating, with photovoltaics and wind energy covering the large majority of all new RES installations.

Wind energy is expected to significantly grow thanks to stable and rewarding policies worldwide, both onshore and offshore [1], and multiple plans have been developed worldwide to sustain it, the most recent example being the announcement of a European Wind Power package by the European Commission President Ursula von der Leyen at the State of the Union 2023 [2]. Offshore wind energy, in particular, is growing in popularity as it offers many advantages compared to its counterpart. First, the IEA estimates that the technical potential could reach 420000 TWh of electric energy produced per year [3], around eleven times the estimated global electricity demand by 2040, and it is currently largely untapped. This estimation is really promising, considering that International Renewable Energy Agency's (IRENA) 2023 report on offshore wind scale-up states that 500 GW of installed capacity will be needed by 2030 to meet the Paris Agreement and Glasgow Climate Pact goals [4]. Not only the technical potential is high, but the average speed of offshore wind is also significantly larger than onshore at the same height, as reported by Archer and Jacobson [5]. Offshore installations also allow for larger dimensions of the rotor, that simultaneously increase the efficiency and improve the economical performance, which supports the current trend to go towards bigger turbines. As fixed-bottom wind turbines costs rapidly increase along with sea-depth, as found in Butterfield et al. [6], Floating Offshore Wind Turbines (FOWTs) represent the most cost-effective approach for deep sea areas, which are usually considered to have a bathymetry higher than 60m. Furthermore, FOWT can also reduce visual and noise pollution, both compared to onshore and near offshore installations [7].

As FOWT show different advantages and they represent the only viable solution at higher bathymetry, numerous designs were proposed in recent years, revealing a lively research field. FOWTs are generally composed by the wind turbine, a floating platform, and mooring lines that hold the structure in place. They are usually divided in three categories, according to how they are stabilized by the floater: mass-stabilized structures (also called spar-type), buoyancy stabilized structures (also called semi-submersible), and Tension Leg Platforms (TLPs). Each design has advantages and disadvantages in terms of performance, costs, and construction methods, e.g. semi-submersible platforms show lower pitch and roll motions compared to spar-type platforms [8], so that some of them may perform better than others in certain environmental conditions. Therefore, it is currently not possible to determine which solution is going to be prevalent in the future.

Nonetheless, the recent history of FOWTs has seen some important milestones, that are commonly taken as reference in the corresponding scientific literature. For example, spar-type platform Hywind Demo has been the first multi-MW FOWT installation in the world [9] and it notoriously led the Scottish government to grant FOWT installations off the Peterhead coast [10]. The Hywind system was also the key solution studied in the Offshore Code Comparison Collaboration (OC3) initiative [11]. However, the Offshore Code Comparison Collaboration Continuation (OC4) moved to DeepCWind project's semi-submersible design [12], which was then slightly modified for Offshore Code Comparison Collaboration, Continued, with Correlation (OC5) [13]. All these projects aimed at improving the knowledge and the expertise in the offshore wind field and they all answered to IEA Wind's tasks aimed at advancing wind energy deployment. Similarly, VoltornUS-S semisubmersible platform was developed by the University of Maine [14] as a reference platform for IEA's reference 15MW wind turbine, under IEA Wind TCP Task 37 [15]. This platform is the perfect example of the sector's trend towards larger rotors, as IEA's 15 MW turbine is currently the biggest and most powerful reference turbine available today.

However, the design and deployment of FOWTs presents some unique challenges, some of which have not been solved yet. A crucial problem is represented by the complex environmental loading due to the action of the wind, waves, and currents, as pointed out for example by Tran and Kim [16]. Not only structural loads can represent a risk for the turbine integrity, but external forces also determine a more complex dynamic behavior of the structure, affecting the operation of the rotor and the capability of the turbine to extract power from the wind. Compared to onshore or offshore bottom-fixed turbines, FOWTs also require a more complex control strategy,

that must account for the turbine's movement with reference to the incoming wind. Therefore, the design phase of FOWTs is crucial in order to ensure the best performance, thus minimizing risks and maximizing profit. As highlighted in a LIFES50+ report [17], this step is in fact a multidisciplinary problem and various authors tend to focus on a small number of selected objectives at a time, e.g. the hull shape optimization or the inclusion of advanced control strategies. These studies always refer to numerical models, as they are a cost-efficient way to perform a high number of tests. Experiments on full-scale or scaled prototypes are still necessary in order to confirm numerical results, and different examples are available in the literature, e.g. tests by Viselli et al. on the VoltturnUS platform [18], [19]. However, full-scale tests are very expensive, and scaled prototypes face the limitations imposed by the need to simultaneously satisfy Froude and Reynolds scaling laws, that make it hard to perfectly represent the full-scale structure. Therefore, numerical simulations are the preferred choice in the design phase as they allow for in-depth investigations of design choices, operational conditions, etc. even though they require careful preliminary studies in order to determine the best equations and algorithms to be used.

In this context, this thesis is the result of a collaboration with Marine Offshore Renewable Energy (MORE) Lab at Politecnico di Torino and it focuses on the effect of accurately estimated damping coefficients on the annual energy production evaluation for a FOWT. In particular, UMaine's VoltturnUS-S Reference semi-submersible Platform is taken as a reference, coupled to IEA's 15MW reference wind turbine, as it is the perfect example of the current offshore wind energy industry's trend towards larger and more powerful systems. The turbine productivity estimation requires an accurate modelling of the structure's interactions with wind and waves, that will be performed in OrcaFlex [20], a cutting-edge software for the dynamic analysis of offshore marine systems. As the semi-submersible platform has a complex geometry, it is crucial to accurately describe its dynamic properties, that will serve as an input for the OrcaFlex model. For structures presenting a complex geometry, it is common practice to include more refined models in lower-fidelity tools like OrcaFlex, that improve the quality of the results by using accurate descriptors obtained from higher-quality and more computationally expensive methods. Therefore, this work will start with a Computational Fluid Dynamics (CFD) simulation of the semi-submersible structure through the commercial software Star-CCM+ [21], posing particular attention on the free decay of the platform for the pitch and heave motions. Special attention is given to the Verification and Validation (V&V) process, in order to evaluate the quality of the results. CFD simulations will be followed by an accurate investigation of the model, in order to optimize the simulation setup in terms of computational time and accuracy. Various tests will

focus on the effect of different mesh parameters, simulation strategies and numerical models. Post-processing techniques based on previous works by members of MORE Lab are then applied to the results of these tests in order to extrapolate an accurate set of linear and non-linear damping coefficients for the platform. Finally, these values will be used in the OrcaFlex model to check their effect on the productivity estimation and on other key descriptors of the system performance. In particular, the FOWT behavior will be simulated using a set of representative real-world data of wind and waves.

# Literature review

As various research projects already focused on FOWT design and testing, a preliminary literature review is necessary in order to draw a faithful image of the current development stage of the offshore wind energy industry. The following paragraphs will give an overview of previous studies, describing what has already been done in order to identify possible areas of investigation. As offshore wind energy extraction is a vast topic, this review will focus on recent developments in the numerical modelling of FOWTs.

The design, testing, and deployment of FOWTs are notoriously challenging tasks due to a plethora of problems that need to be carefully addressed and solved. In the literature, different authors identify different obstacles, according to the objective of their research, but they are often related to fluid-structure interactions. One of the most prominent problems in FOWT modelling is the complex load coupling of aerodynamics, hydrodynamics, and structural dynamics, as highlighted for example by Tran and Kim [16]. Moreover, Luo et al. [22] remark that the interaction between the rotor motion and the floater motion makes the control strategy design even more difficult. The same authors also underline that the aerodynamic load of wind and the hydrodynamic load of waves are generally stochastic, adding another layer of complexity to the implementation of advanced control strategies. Load coupling and control strategies are tightly connected to the dynamic response of the FOWT, which already poses its own challenges. For example, the aerodynamic force on the rotor is transmitted through the tower to the support platform, affecting its dynamic response. At the same time, mooring lines restrict the movement of the platform. As the platform moves, it affects the relative flow velocity seen by the rotor, and it can even generate complex situations that are hard to numerically describe, e.g. the rotor might move in the direction of the wind, thus traversing its own wake [16], [23].

In the next paragraphs, the numerical modelling of FOWTs will be explored through the analysis of a representative sample of publications about the topic. After a brief introduction on the numerical models needed to correctly describe the physics of a FOWT, the main modelling choices of each publication will be highlighted. This process is necessary in order to investigate already tested techniques and their results, highlighting promising trends and common practices. Finally, the next paragraph will focus on the Verification and Validation (V&V) process, as it is sometimes overlooked by authors, despite its importance as an indicator of the reliability of the results.

## **The modelling of a FOWT and the evaluation of its characteristics**

As introduced in the previous section, a FOWT deals with aerodynamic and hydrodynamic loads at the same time. Therefore, as the goal is to describe the behavior of a FOWT in a real environment, it is impossible to consider the tower and the rotor separately from the floating support platform and the mooring lines. However, each of these elements plays a precise role and it must be carefully designed and studied. The analysis of each component as well as of the entire structure can be performed with different tools, that provide different degrees of accuracy and require different computational times. Several software packages allow engineers and researchers to perform time-domain and frequency-domain analyses using simplified methods, e.g. strip theory and panel methods. Some examples include: ANSYS AQWA[24], WAMIT [25], OrcaFlex [20], FAST (Fatigue, Aerodynamics, Structures, and Turbulence) and its most recent adaptation OpenFAST [26] (in particular, for documentation on the Hydrodyn module see: [27]), OpenFOAM [28], and STAR-CCM+. In general, higher-fidelity analyses like CFD are more complex and require more time, but they provide better-quality results, that can then be used in lower-fidelity tools for faster calculations.

In the last decades, a strong research effort has led to noticeable improvements in the field of numerical modelling of FOWTs. One of the most prominent advances in the field is the development of fully coupled aero-hydro-elastic analysis tools and methods that allow researchers to test floating platform designs in significant Design Load Cases (DLCs), to investigate fluid-body interactions in detail, as well as to obtain key descriptors of the dynamic response of the FOWT. These tools aim at solving the behavior of the entire system, but they usually do so by splitting the problem in its core elements. For example, they might include a module to solve for aerodynamics interactions, another module to solve for hydrodynamics interactions, and other modules for structural loads, mooring lines, etc. They then implement a method to make these modules communicate with each other at each time instant.

Aerodynamic analysis tools and methods have benefited from the onshore wind industry development over the years. They include the Blade Element Momentum (BEM) theory defined by Glauert [29], vortex methods defined by Voutsinas et al. [30], methods based on potential flow theory like the one by Van Bussel [31], the Actuator Line Method (ALM) by Shen and Sørensen [32], and various CFD methods, e.g. by Zhou and Wan [33]. Each of these methods has its own advantages and disadvantages, and even the oldest ones still find application in commonly used engineering tools, e.g. the AeroDyn module in the National Renewable Energy Laboratory's (NREL) tool OpenFAST based on quasi-steady BEM theory [26], [34]. Compared

to onshore turbines, the aerodynamic analysis of an FOWT is more complex, due to the floating platform response. For example, there are studies on unsteady aerodynamic interference predictions by Tran et al. [16], [35]–[37], investigating the complex effect of surge, pitch and yaw motion on the aerodynamic loads and on the wake. As aerodynamic loads and interactions will not be included in this work, the corresponding analysis methods will not be further described. More details on this decision can be found in the next chapter, where the assumptions and setup choices for the simulation will be listed.

From the point of view of this thesis, which concentrates on hydrodynamic damping coefficients estimation based on free decay tests, hydrodynamic analysis tools are more relevant. A lot of different methods are available, but not all of them are suitable for all applications. Traditional engineering models have known large success in the Oil and Gas sector for offshore platforms, and they include, for example, tools based on potential-flow theory. Although they are faster and easier to use, they are inevitably less accurate. A well-known limit of potential-flow-based tools is that they do not include viscous effects, which is usually solved with additional damping coefficients (obtained from experiments or higher-fidelity tools) or with Morison's equation, based on strip theory. More sophisticated hydrodynamics effects are included through empirical models and correction factors, thus being less reliable when used to simulate a structure's behavior outside of the environmental conditions for which the correction terms were developed. This is where higher-fidelity tools become important, particularly CFD/6-Degrees of Freedoms (DOFs) tools. In general, this solution only requires knowledge about the structure geometry and mass properties to simulate a wide variety of situations. However, solving the problem becomes more complex and an in-depth knowledge of models and techniques is often necessary in order to avoid issues such as numerical divergence. Moreover, CFD simulations are characterized by long computational times and, in some cases, they might require powerful hardware, e.g. if Large Eddy Simulation (LES) or Direct Numerical Simulation (DNS) approaches are chosen.

Finally, most tools include mooring modelling, as it is necessary to restrain the motion of the platform and it allows for the simulation of real operating conditions. Mooring lines constitute a limit for translational motions, but they also act as additional restoration forces for rotational motions. Different modelling strategies include quasi-static approximations and dynamic models such as lumped-mass representation, finite-element analysis through space discretization of the line, and finite difference models both in space and time [38]. Providing a faithful representation of the mooring lines behavior is a complex task as different physics

descriptions must be included such as inertial effects, internal damping, bending, and torsion. Different tools are available, and others are created *ad hoc* by researchers to be included in more complex software packages. A non-exhaustive list includes: MoorDyn module in OpenFAST [39], MOORING3D [40], Ansys AQWA, the quasi-static model in Liu et al.'s tool [41], and the Maritime Research Institute Netherlands (MARIN) in-house solver aNySIMxmf [42]. However, modelling the mooring lines can add complexity to the solver and sometimes it is necessary to remove them, as reported for example by Dunbar et al. when testing the FAST Certification Test cases [43]. As mooring lines will not be included in this work, no more details will be given about the corresponding modelling techniques, but this choice will be discussed again in the next chapter.

## **Examples of FOWT modelling**

Even though the description of the behavior of the tower and platform together is out of the scope of this work, related publications are rich in relevant results. Before continuing, it is necessary to notice that the cited works focus on specific platform designs, which may differ from the one analyzed in this study. However, the proposed methods can be generalized to most cases regardless of the technological solution they were originally tested on. In the following section, the comparison of these methods will highlight the most promising techniques and it will serve as a theoretical basis for the analysis that will be conducted in the next chapter.

Among semi-submersible platforms for FOWTs, the OC4 DeepCWind platform is certainly one of the most studied, usually coupled with NREL 5 MW reference baseline wind turbine. Tran and Kim performed an extensive work, the results of which are reported in different papers [16], [23], [35], [44]. In one of their first publications [44], they focus on the simulation of free decay of the platform in all 6 DOFs and the evaluation of the corresponding natural frequencies. They perform their simulations using the CFD software STAR-CCM+ with an overset grid technique, to manage large body motions. The same technique was applied in their next publications [16], [23], as their results confirm that CFD simulations are more accurate than potential-flow-based ones. The water free surface is treated through the Volume of Fluid (VOF) method [45]. All other publications cited in this paragraph will use the VOF method, unless stated otherwise. While discussing viscosity effects on surge free decay motion, the authors compared 5 cases: an inviscid fluid model, a laminar flow treatment, the  $k-\omega$  Shear Stress Transport (SST) turbulence model, the Spalart-Allmaras turbulence model, and the  $k-\epsilon$  standard turbulence model [44], [46]–[48]. Only the  $k-\epsilon$  model results do not compare with experimental data, while all other models yield similar results. The authors also dedicated an article to the

implementation of a Dynamic Fluid-Body Interaction (DFBI) approach [23]. From the comparison with other solvers, they found that their DFBI approach provides the most similar results compared to experimental data.

Dunbar et al. [43] developed a tightly coupled CFD/6-DOF solver based on the open source CFD toolbox OpenFOAM [49], although they do not provide additional information on their simulation setup. Benitz et al. modelled the same platform in OpenFOAM, applying the Spalart-Allmaras one equation turbulence model [50]. Liu et al. [41] developed another tool based on OpenFOAM. As the authors point out, the overset grid technique is a common practice in FOWT simulation, but it often requires obtaining a license for commercial CFD software packages. Therefore, they applied OpenFOAM built-in sliding mesh technique called Arbitrary Mesh Interface (AMI). They then employed the  $k-\omega$  SST turbulence model. Cheng et al. further developed an OpenFOAM CFD solver for hydrodynamics problems [51], named naoe-FOAM-SJTU, to be coupled with an aerodynamics solver to create a fully coupled solver for the analysis of the entire FOWT. The naoe-FOAM-SJTU solver uses the Finite Volume Method (FVM) to discretize the computational domain, and the dynamic deformation mesh approach to deal with the platform motion.

OC5 DeepCWind semi-submersible floater is instead the object of Wang et al. [52] and Burmester et al. [53] publications. They both employed the community-based open source CFD code ReFRESKO [54], with a deforming-grid method from de Boer et al. [55] and a moving-grid method, respectively. They also apply the KSKL ( $k - \sqrt{k}L$ ) turbulence model [56], as they claim it shows an advantage in the convergence of the residuals compared to the  $k-\omega$  SST model. The free surface is still modeled using the VOF method, confirming its efficacy, but Wang et al. refer to the VOF modification introduced by Klajj et al. [57].

The UMaine VoltturnUS-S reference platform has been thoroughly defined in 2020 by NREL in a technical report [14], which is among the most complete studies on this platform available today. In the report, frequency-dependent coefficients for OpenFAST have been evaluated through the boundary-element-method hydrodynamics solver WAMIT v6. The viscous damping matrix for all 6 DOFs has been obtained, on the other hand, using OpenFOAM. In particular, they used the steady-state, incompressible solver version of the software, i.e. SimpleFoam [58]. Rigid body free decay simulations have then been performed in OpenFAST for all 6 DOFs. Therefore, these simulations are affected by the well-known limitations of the potential-flow-based method of FAST. Even though the free decay tests are run including correction factors for viscous damping which come from a CFD analysis, these coefficients have

been obtained by considering the net drag load on the body due to the fluid moving around it. A new evaluation of quadratic damping coefficients is needed in order to compare results and highlight possible differences between the two methods. Numerical aeroelastic hydrodynamic coupled models are employed by Viselli et al. [59] to predict the response of the full-scale VoltornUS platform with a 6MW turbine. In particular, they primarily used FAST version 7, together with ANSYS AQWA Release 14.5 that was added to evaluate mooring tensile loads. Neither this publication nor the previous work by Allen et al. [60] add information on these models that would be relevant for the present work, except for reminding the inclusion in the FAST model of the quadratic drag model in the form of a quadratic damping matrix.

Various other papers deal with the numerical modelling of FOWTs, both in the semi-submersible category and the spar or tension leg platform (TLP) categories. Philippe et al. developed a hydrodynamic model of loads to be integrated in FAST, substituting the built-in HydroDyn model, and tested it on the Dutch Tri-floater semi-submersible concept [61]. Beyer et al. [62] coupled the CFD code ANSYS CFX [63] with the Multibody System (MBS) software SIMPACK [64]. CFX is used to evaluate flow-induced hydrodynamic loads, and the simulation setup includes a moving mesh methodology and the  $k-\omega$  SST turbulence model. Simulations on the OC3 – Hywind spar-buoy floating platform are used to compare the new solver to other existing alternatives based on linear hydrodynamics. The same floater is modelled by Quallen et al., with a focus on the mooring line modelling [65]. They used URANS finite-difference solver CFDShip-Iowa V4.5 [66], with an overset technique. They are the only ones in this review not to use the VOF model, as they employ a level set method from Carrica et al. instead [67].

## **Verification and validation of numerical models**

In the previous paragraph, the focus was the choice of different solvers or modelling techniques in the numerical simulation of FOWTs. However, any numerical investigation needs to be accompanied by an appropriate verification and validation (V&V) procedure, and the results should preferably be reported along with an uncertainty interval. V&V methods, as well as uncertainty evaluation techniques, will be discussed in detail in the following chapter. Nonetheless, a short review of the cited works is deemed necessary in order to assess the quality of the published results, as well as to identify common practices.

As Roache notoriously wrote in his book *Verification and Validation in Computational Science and Engineering*, “we adopt the succinct description of ‘Verification’ as ‘solving the equations right’ and of ‘Validation’ as ‘solving the right equations’ ” [68]. Therefore, verification

is related to correctly solving the equations included in the model, so it needs a comparison with analytical results or forcing another code to solve the same set of equations for the same benchmark problem. Some papers for example compare their solver to FAST, although it is not a CFD solver and it needs correction factors in order to include all the necessary physics. The verification step should be followed by a convergence study on the discretization step size(s) selected to numerically solve the equations. Validation, instead, is related to solving the right set of equations, i.e. it is needed to verify whether the model includes all necessary physical phenomena. Therefore, numerical results must be compared to experimental data for the same simulated problem. When a proper experimental setup cannot be put in place, it is possible to perform validation through numerical results from another validated code, although in that case this step does not correspond to verification too. Both experimental and computational data used as comparison term for validation should be accompanied by errors and uncertainties for the entire process to be as accurate as possible. From a different point of view, it could be said that verification is related to numerical uncertainties, while validation is related to modelling errors.

As most of the cited publications use existing verified codes, they tend not to perform a verification step, even after they coupled them to additional in-house solvers. Dunbar et al. are among the few to perform and document a verification process for their OpenFOAM-based solver [43], using it to simulate the benchmark case of heave free decay of a 2D circular cylinder. The solver is then validated with a theoretical solution for the same problem. When they applied the solver to the DeepCWind case, they only validated the results by comparing them to numerical results from FAST, highlighting and justifying differences between the two. Noticeably, the authors performed a grid size and a time-step size convergence study, for the heave free decay simulation of both the 2D circular cylinder and the FOWT platform.

Wang et al. perform a thorough V&V process too [69], however, they do not verify their model against a benchmark problem as Dunbar et al. did. Instead, as there is no analytical solution for the response of a semi-submersible floater under regular waves, they perform the verification step by estimating the numerical uncertainty in order to determine an interval containing the exact solution with a 95% confidence. As it will be seen, convergence studies and uncertainty estimation are the most common way to perform verification. As for validation, Wang et al. refer to Coleman and Stern's approach [70] and they use experimental data and the evaluated uncertainty from Robertson et al. [71].

Wang et al. [52] and Burmester et al. [53] both focused on free decay modelling using CFD code ReFresco, publishing results on pitch and surge motion, respectively. They both perform

a thorough V&V analysis. With reference to the first negative oscillation peak, they both perform convergence studies and uncertainty estimation. Wang et al. only test three meshes, while Burmester et al. test three spatial grids and use three time-step values. In order to extrapolate the exact value of the quantity of interest, Wang et al. apply Roache's GCI procedure [72] whereas Burmester et al. apply Eça and Hoekstra method [73]. Both of them validate their results against experimental data, even though no error or uncertainty accompanies them.

Tran and Kim performed their simulations in STAR-CCM+ coupled with user-field functions [16]. They could count on previous studies in which different simulations were compared against conventional simulation tools and in which they performed a grid dependency test and a time-step convergence study [35]–[37], [74]. As they report, verification and validation had been previously performed for both free decay and regular wave conditions using other codes and MARIN experimental data, respectively [44]. The fully coupled aero-hydrodynamic simulations of the full-scale platform are validated against FAST results, although no error bands are reported [16]. In their DFBI approach-based analysis, they successfully completed convergence tests using the time-step size and validated the results against experimental and numerical data [23].

Cheng et al. validated each module of their solver separately [51]. They refer to Zhao and Wan's publication for verification and a grid convergence study on the naoe-FOAM-SJTU solver, although repeating the convergence study is always recommended, e.g. to check whether the asymptotic range has been reached for some relevant fluid flow quantity. The naoe-FOAM-SJTU solver is validated by Cheng et al. against experimental data and numerical results from FAST, taken from Coulling et al. [75], and from other CFD solvers [23], [41], [44], [76], [77]. On their behalf, Liu et al. validated their tool against a similar set of publications [23], [41], [44], [75], also reporting a mesh sensitivity test.

The NREL technical report on VoltturnUS-S reference platform does not seem to report any detail on verification, validation, or uncertainty [14]. Viselli et al. successfully validated their FAST and ANSYS AQWA simulations against experimental data for the 1:8 scale prototype of VoltturnUS platform (VoltturnUS 1:8) deployed offshore Maine [59], although a more detailed description of a validation process must be looked for in Allen et al. [60]. Neither of these two publications report an evaluation of the uncertainty on the numerical results, nor they include experimental uncertainty. A custom FAST model had previously been validated by Viselli et al. against experimental data for the 1:8 scale prototype, but the uncertainty on the experimental data is not reported [19].

Beyer et al. do not perform any verification step, but they report a comparison between the coupled solver (MBS+CFD), a version of the solver with the MBS module and HydroDyn, and finally with FAST [62]. Given that SIMPACK is a validated aero-servo-hydro-elastic simulation tool for wind turbines, it is assumed it has been verified and thus the comparison could be used as a validation step. Similarly, Quallen et al. do not verify their solver, nor they run any test on the discretization parameter, but they compare their results to a FAST simulation for validation [65].

As they use OpenFOAM, Benitz et al. do not conduct a verification of the code, but they also neglect convergence studies [50]. They still compare their results to experimental data and numerical solutions from other solvers from various sources.

Philippe et al. did not perform V&V, and they do not report uncertainties on their numerical results nor complete any discretization step convergence study [61]. Even though their results seem to align with the findings of many other publications, objections could be raised against the use of a non-verified and non-validated in-house model.

# Free decay simulations

As it will be explained in the next chapter, the evaluation of damping coefficients for VoltturnUS-S platform will be performed based on the results of free decay simulations for the same FOWT configuration. A high-fidelity CFD approach has been chosen in this work to complete free decay simulations for the pitch and heave DOFs. Therefore, this chapter will first introduce the geometry of the platform. Then, for each DOF, different paragraphs will follow the simulation setup, carefully explaining all choices and bringing to the attention of the reader any source that could justify the most important decisions. As the quality of any successive analysis primarily depends on the quality of the results of the CFD simulations, convergence studies for both the space and time discretization parameters are reported in this chapter in order to verify the numerical model. The pitch case has also been taken as reference to perform an accurate investigation of the numerical setup. In particular, the effect of individual solvers and their internal options is checked in order to assess whether they are useful to improve the quality of the results. As CFD free decay simulations are known to require a significant amount of time to be concluded, this detailed discussion will also aim at minimizing the computational time.

## **VoltturnUS-S platform geometry, mesh generation and boundary conditions**

The focus of this work is the VoltturnUS-S semi-submersible platform, a representation of which can be seen in figure (1) (source: [14]), along with the reference coordinate system and the 6 DOFs. The platform geometry is the result of the research work conducted at the University of Maine, which also includes numerical modelling and at-sea testing of a scaled version of the platform. As reported by various publications, the platform design aimed at investigating different innovative strategies including new materials and towing strategies [18], [19], [59]. The semi-submersible platform comprises four steel columns, one central and three radial. The radial columns are evenly spaced by  $120^\circ$  and they are each connected to the central column by a stiff brace at the base. Smaller connections are present in the original model, but they have not been included in this study in order to simplify the geometry and thus the mesh. Moreover, previous studies pointed out that the contribution of these thin elements to the overall performance of the system is marginal [50]. The platform has been designed to work with the IEA-15-240-RWT turbine, i.e. IEA's 15 MW reference offshore wind turbine [15], which is plausibly the largest reference turbine model available today.

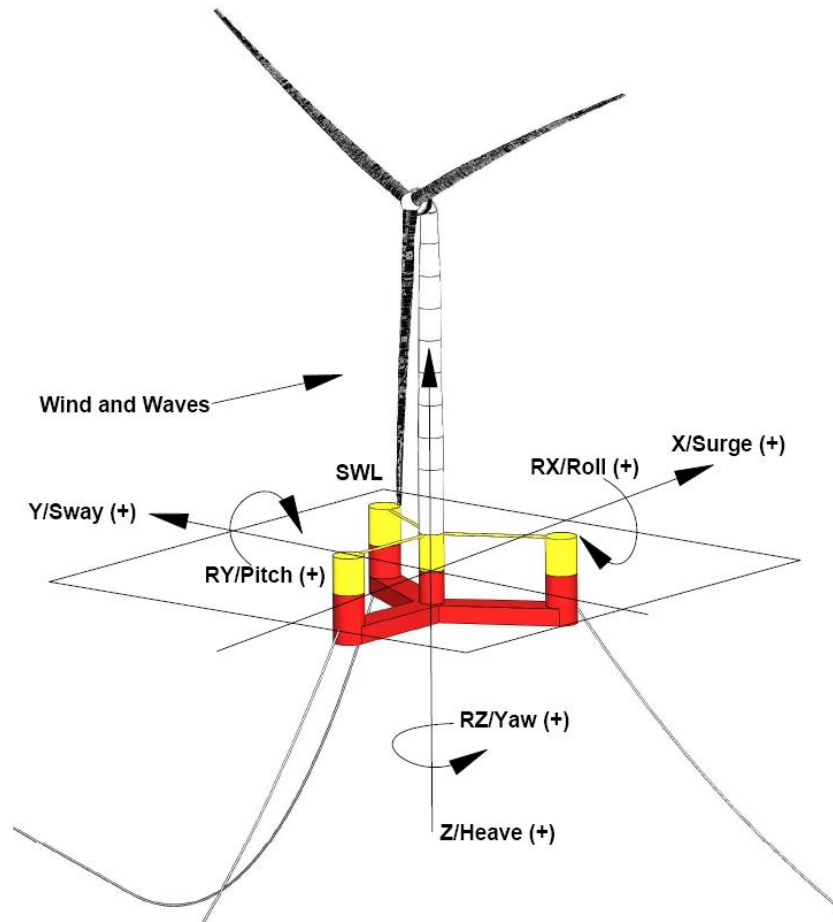


Figure 1 - VolturnUS-S platform and IEA's reference turbine, highlighting the reference coordinate system (source: [14]).

In the following simulations, only the floating platform is modelled in STAR-CCM+, for a number of reasons. First of all, only free-decay simulations are run, i.e. the platform moves in the absence of both wind and waves. As in this case the turbine rotor can be assumed to be still, the entire turbine, including the rotor, the nacelle, and the tower, is eliminated from the 3D model of the FOWT system. Even though in a real situation friction forces due to the air have a small effect on the tower response, their impact on the result is considered negligible and thus they are ignored by completely removing the tower. As the tower is over 100m high, this choice helped largely reducing and simplifying the computational domain. This decision was also supported by the evidence brought by other previously discussed works, such as Wang et al. [69], Tran and Kim [23], Benitz et al. [50], and Wang et al. [52]. However, the mass and inertia properties of the tower are still included in the simulation. As a result, even though the modelled geometry only represents the floater, properties like the mass, the center of mass, and the draft refer to a system

in which the turbine is present. A summary of the platform properties, adapted from the IEA’s technical report [14], can be seen in table [1].

A further simplification can be found in the elimination of the symmetrical mooring lines that hold the platform in place. This choice comes at a cost, as the surge (and sway) free decay motion can no longer be simulated. However, it helps reducing the computational cost of each time step of the pitch and heave simulations. At the same time, running the simulation without mooring lines has the effect of providing results that are strictly linked to the properties of the platform and the tower, rather than being the sum and the mix of all contributions. Future studies should be conducted to include and compare relevant mooring lines models in order to isolate their contribution to the FOWT’s dynamic response.

Table 1 - General system and semi-submersible platform properties (adapted from: [14]).

<b>Parameter</b>	<b>Units</b>	<b>Value</b>
<b>General system properties</b>		
<b>Platform type</b>		Semi-submersible
<b>Freeboard</b>	m	15
<b>Draft</b>	m	20
<b>Total system mass</b>	t	20,093
<b>Platform mass</b>	t	17,839
<b>Tower mass</b>	t	1,263
<b>RNA mass</b>	t	991
<b>Semi-submersible platform properties</b>		
<b>Hull displacement</b>	m <sup>3</sup>	20,206
<b>Hull steel mass</b>	t	3,914
<b>Tower interface mass</b>	t	100
<b>Vertical center of gravity from SWL</b>	m	-14.94
<b>Vertical center of buoyancy from SWL</b>	m	-13.63

## **Pitch free decay**

The pitch free decay simulation has been run first, followed by the corresponding convergence studies. This simulation has also been taken as reference for in-depth investigations of the effect of some solver choices, aiming at minimizing the computational time without sacrificing the accuracy. All studies and investigations refer to the same free decay case in which the floating platform is initially tilted by  $-10^\circ$ .

Three techniques are generally available to solve Navier-Stokes Equations (NSEs): Direct Numerical Simulation (DNS), that tries to directly solve the equation and thus all motions in the flow; Large Eddy Simulations (LES), where NSEs are filtered only over space; Reynolds-

Averaged Navier Stokes (RANS), that splits flow quantities in a mean value and a perturbation value. Unsteady RANS (URANS) has been selected as it is cost-efficient in terms of computational time, which would increase by some orders of magnitude if LES or DNS were used. NSEs are reported in equations (1,2), while the URANS modification is reported in equations (3-6). URANS equations are reported for an incompressible fluid, and they have to be coupled with the time-averaged equation for the transport of a generic scalar quantity  $\phi$ , as in equation (7). In these equations  $\rho$  is the density of the fluid and  $p$  is pressure. In the URANS equations, capital letters  $U$ ,  $V$ , and  $W$ , represent each steady mean velocity component, while lower case letters with an apex represent the corresponding time-varying fluctuating component.

$$\left\{ \begin{array}{l} \frac{\partial \rho}{\partial t} + \nabla \cdot (\rho \mathbf{U}) = 0 \\ \frac{\partial (\rho \mathbf{U})}{\partial t} + \nabla \cdot (\rho \mathbf{U} \mathbf{U}) = \mu \nabla^2 \mathbf{U} - \nabla p + \rho \mathbf{g} \end{array} \right.$$

(Eqs. 1,2)

$$\left\{ \begin{array}{l} \nabla \cdot \mathbf{U} = 0 \\ \frac{\partial U}{\partial t} + \nabla \cdot (U \mathbf{U}) = -\frac{1}{\rho} \frac{\partial p}{\partial x} + \nu \nabla \cdot (\nabla(U)) + \frac{1}{\rho} \left[ \frac{\partial (-\rho \overline{u'^2})}{\partial x} + \frac{\partial (-\rho \overline{u'v'})}{\partial y} + \frac{\partial (-\rho \overline{u'w'})}{\partial z} \right] \\ \frac{\partial V}{\partial t} + \nabla \cdot (V \mathbf{U}) = -\frac{1}{\rho} \frac{\partial p}{\partial y} + \nu \nabla \cdot (\nabla(V)) + \frac{1}{\rho} \left[ \frac{\partial (-\rho \overline{u'v'})}{\partial x} + \frac{\partial (-\rho \overline{v'^2})}{\partial y} + \frac{\partial (-\rho \overline{v'w'})}{\partial z} \right] \\ \frac{\partial W}{\partial t} + \nabla \cdot (W \mathbf{U}) = -\frac{1}{\rho} \frac{\partial p}{\partial z} + \nu \nabla \cdot (\nabla(W)) + \frac{1}{\rho} \left[ \frac{\partial (-\rho \overline{u'w'})}{\partial x} + \frac{\partial (-\rho \overline{v'w'})}{\partial y} + \frac{\partial (-\rho \overline{w'^2})}{\partial z} \right] \end{array} \right.$$

(Eqs. 3-6)

$$\frac{\partial \phi}{\partial t} + \nabla \cdot (\phi \mathbf{U}) = \frac{1}{\rho} \nabla \cdot (\Gamma_{\phi} \nabla(\phi)) + \left[ -\frac{\partial (\overline{u' \phi'})}{\partial x} - \frac{\partial (\overline{v' \phi'})}{\partial y} - \frac{\partial (\overline{w' \phi'})}{\partial z} \right] + S_{\phi}$$

(Eq. 7)

RANS method needs to be closed with additional equations, which fall in the turbulence models group. The setup must also be integrated with additional models, e.g. to deal with water free surface and large body motions, that need to be thoroughly discussed. In the following sections all simulation choices will be carefully illustrated, from the mesh creation to the setting of the boundary conditions and the selection of proper solvers and methods. The adopted methods for data post-processing, like Richardson's Extrapolation (RE), will also be discussed. After that, the convergence study for the spatial parameter and the time step will be conducted. This will set the bases for the investigation of the role of each solver, to optimize the simulation

and cut the computational time. The results obtained from the definitive version of the model will be reported and discussed in the next chapter, together with the ones obtained during the heave simulation.

### **Mesh generation and boundary conditions**

As the platform geometry has already been defined, it is possible to discuss the computational domain and the mesh generation process. It is important to notice that mesh generation techniques are common between both the pitch and the heave free decay simulations, but various considerations led to the creation of two different meshes for the two cases. Moreover, in this paragraph only the base case values are reported, i.e. a reference set of discretization parameters that do not account for the result of convergence studies. A discussion on space and time discretization parameter convergence can be found in the corresponding section, in which the best values will be selected.

The computational domain has been built as a parallelepiped (also called “tank” in this work) containing the 3D model of the platform, partially immersed in the water. Therefore, it is already clear that the model will need to simulate the body motion with two fluids, air and water, the properties of which are reported in table [2]. Fresh water properties have been chosen instead of seawater in order to simplify future comparisons with experimental data in wave tanks. The model has been immediately simplified by including only half of the platform, cut along a vertical symmetry plane passing through the centers of a radial column and the central one. This is possible because both the geometry of the platform and its motion are symmetrical, and there is not an external fluid flow or any boundary condition that could break this symmetry. Thanks to this consideration the number of cells can be significantly reduced. The size of the computational domain around the body is then chosen, leaving enough space around the structure for the generated waves to travel far from it without reflecting back, with the help of the boundary conditions explained later in this section. The size of the tank is based on a relevant geometric dimension of the platform, as no waves are present. Therefore, a reference size  $\lambda$  equal to 80m is chosen as it is sufficiently longer than the platform brace length. The tank is then set to be  $6\lambda$ -long (480m) and  $3\lambda$ -wide (240m). The domain is 150m high, and the water depth is set to 100m as FOWTs are usually installed at sea depths greater than 60m. The platform is then placed in its resting position, based on the reference values in table [1]. The resulting look of the tank and half-platform 3D model is shown in figure (2).

Table 2 – Air and water properties used in the simulation.

	Density [kg/m <sup>3</sup> ]	Dynamic viscosity [Pa s]
<b>Air</b>	1.18	1.85E-05
<b>Water</b>	998.2	1.00E-03

Simcenter STAR-CCM+

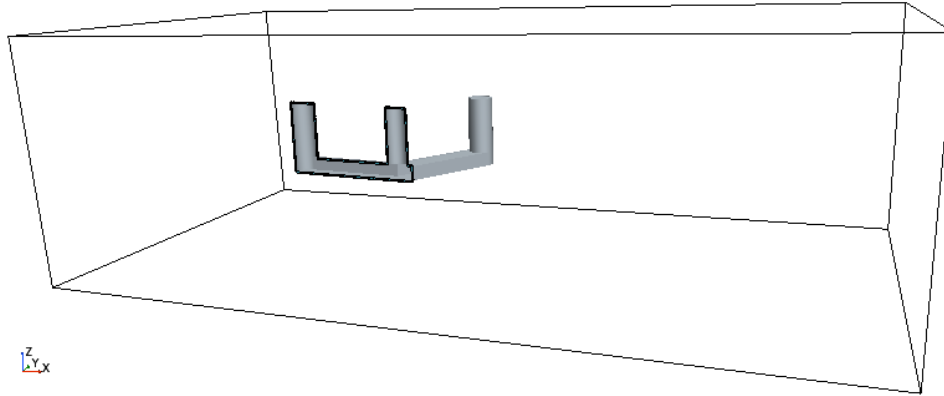


Figure 2 - 3D view of the half-platform 3D model in the computational domain.

The mesh is automatically generated through STAR-CCM+ built-in mesh generator. A triangle Surface Remesher is included, the base size is 100m, the Target Surface Size is equal to 8 times a reference height  $h$  (set to 2m to have enough space to model the water free surface), the Surface Growth Rate is set to 1.05, the Volume Growth Rate is set to 2, the maximum cell size is again  $8h$ , and both the Automatic Surface Repair and Trimmed Cell Mesher are included. In order to reduce the computational weight of the simulation, the grid is progressively refined closer to the structure and it is let coarser far from it. In particular, a cylindrical region is generated, centered on the vertical axis of the platform and with the corresponding radius equal to  $\lambda$ . The region extends from 20m above the still water level (SWL) to 35m below it. In this region, custom controls are set to refine the mesh, so that the trimmer control has the Customize Isotropic Size enabled and the custom size is set as  $8h$  as a percentage of base. A further refinement is set across the water free surface, in order to better simulate the generated waves. In particular, two refinement regions are defined as concentric discs, whose radii are  $1.5\lambda$  (120m) and  $2\lambda$  (160m), while they extend on both sides of the SWL for  $0.7h$  (1.4m) and  $h$  (2m), respectively. An extra region is used in order to smoothen the transition between different cells and reduce reflection during information exchange. It occupies the entire length and width of the tank, and it extends from  $2h$  (4m) above the SWL, to  $40h$  (80m) below it. The Adaptive Mesh Refinement (AMR) method is also applied in this study, which seems to be a *unicum* in the reviewed literature. Deciding where to refine the grid is not trivial, and in transient problems the

most relevant regions may change in time. The refining procedure is more properly part of the solution process, as it is iteratively performed alongside fluid dynamic computations, in order to evaluate each cell's adaptive mesh criteria based on the current flow solution. A more in-depth explanation of the process can be found in STAR-CCM+ guide [21].

The platform large motions are dealt with through the overset grid technique (also called overlapping grid or chimera grid, in other publications). Not only this option is already available in STAR-CCM+, but it is also a common and easy to handle technique, as highlighted in the previous literature review. The computational domain is therefore split in two overlapping parts, called background and overset. The first one is fixed, while the second moves with the body. The fluid dynamic equations are solved separately in the two regions, and then information is exchanged at the interface, i.e. in the overlapping region where the solution is interpolated between *donor* and *acceptor* cells according to [78], [79]. In this study, the overset layer is built so that it is neither too large, as it could cause interpolation errors, nor too small, as cells need to grow from the wall to the tank cells. The overset mesh uses a Polyhedral mesher and a Prism layer mesher. The overset layer is approximately 1m thick. The prism layer uses the Wall thickness option to evaluate the thickness distribution across four layers, with a Prism layer near wall thickness of 0.01m and a Prism layer total thickness of 0.1m. Usually, it would be necessary to tune the wall layer so that the  $Y^+$  parameter is compatible with the turbulence model and the wall treatment model. This requires a preliminary knowledge on the flow characteristics that is hard to obtain for a long and complex simulation of this kind. However, as it will be clearer later in this chapter, STAR CCM+ is quite robust and the selected characteristics of the overset layer will be sufficient for the simulation. Moreover, a uniform selection of the overset layer characteristics made the setup easier, even though in the case of complex flows it could be possible to adjust them in different regions of the domain to account for local flow characteristics.

Figure (3) shows a side view of the generated mesh on the symmetry plane, while figure (4) shows the top view of the mesh at the SWL. Figures (5) and (6) report a detail of the same views to highlight the overset mesh.

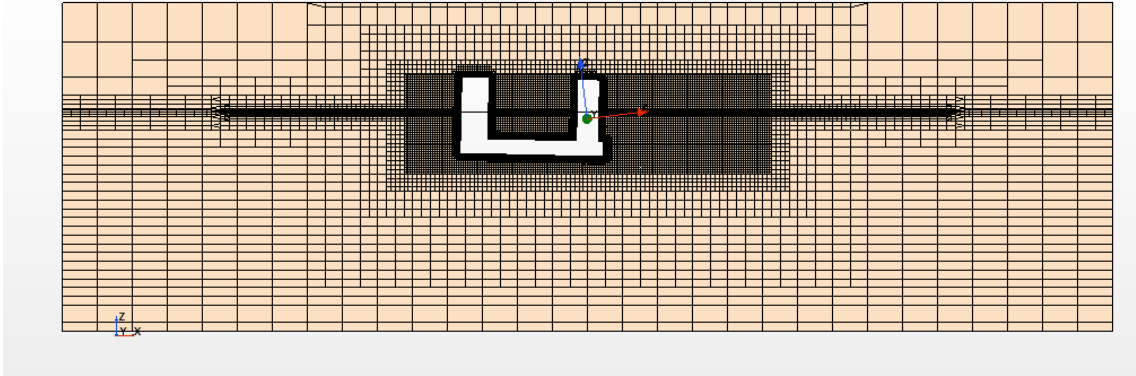


Figure 3 - Side view of the generated mesh for the pitch free decay case.

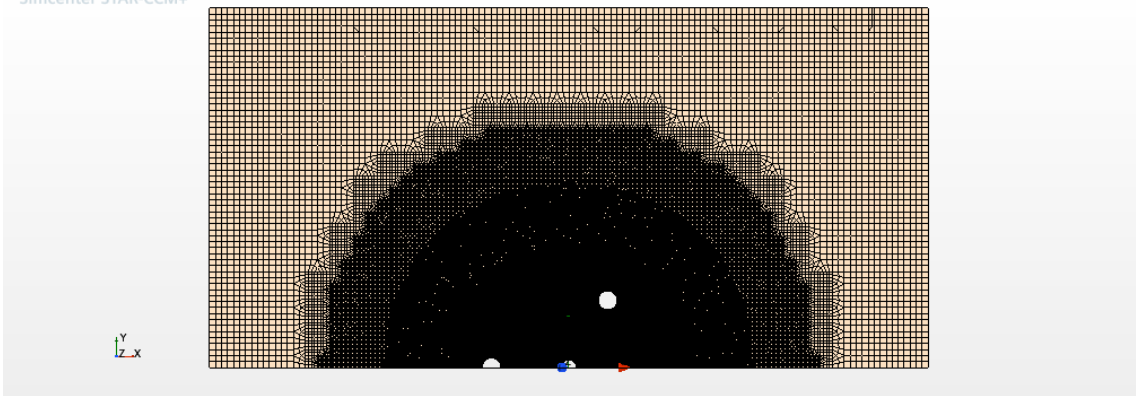


Figure 4 - Top view of the generated mesh for the pitch free decay case.

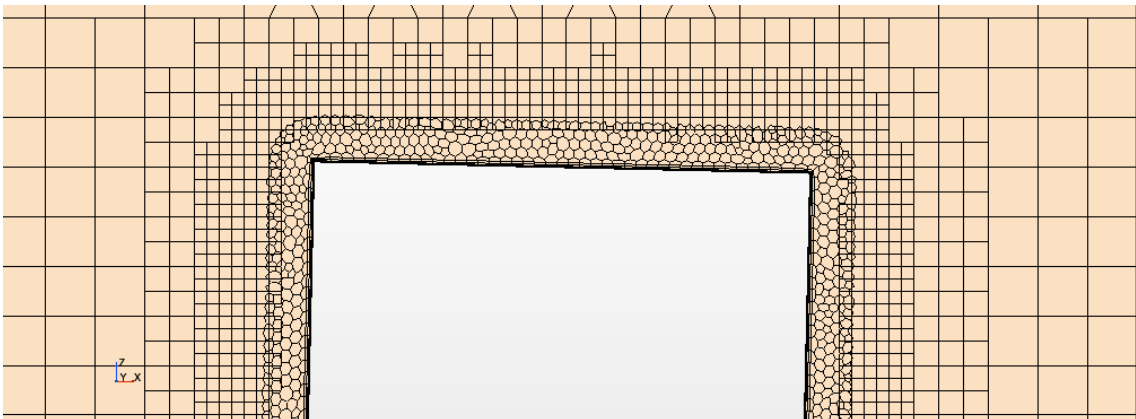


Figure 5 - Detail of the side view of the generated mesh for the pitch free decay case.

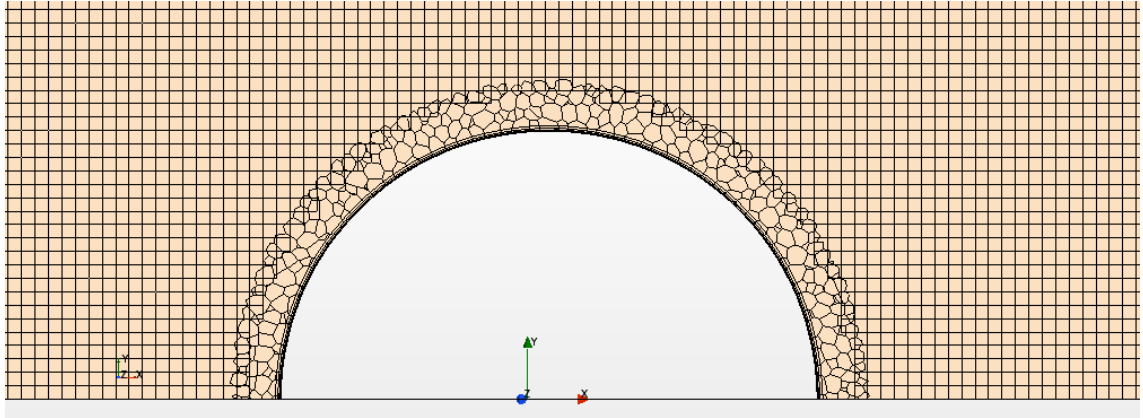


Figure 6 - Detail of the top view of the generated mesh for the pitch free decay case.

Six boundary conditions have to be defined for the tank: a Wall condition on the bottom boundary, a Velocity Inlet on the front, back, and side boundaries, a Symmetry condition on the symmetry plane that is used as boundary, and finally a Pressure Outlet condition on the top boundary. The velocity inlets include a forcing function for waves that is set to zero to improve the damping of the generated waves and avoid reflection. The top Pressure Outlet conditions is, instead, necessary to maintain the default hydrostatic pressure.

### **Time step**

Time discretization requires a separate discussion, as it is linked to the solvers included in the simulation. The VOF model, that is described better later in this paragraph, requires an implicit unsteady approach to solve the pressure-velocity coupling. In the base case, the maximum number of inner iterations is set to eight. Even though first order time discretization would be unconditionally stable, it has a built-in problem linked to artificial diffusivity. In particular, “*the leading term of the truncation error of convective flux resembles a diffusive flux*”, as marked by Fontana et al. [80]. Multidimensional problems where the flow is not aligned to the grid can even exacerbate this flaw, unless a very fine grid is used. Therefore, a second order approach has been selected for this work. Not only it avoids the fine grid requirement, but it is also more accurate than the first order approach. The main drawback is that the time step value is limited by two requirements.

- As highlighted in Fontana et al. [80], the Courant number defined in equation (8) must be at least less than 1 to be compliant with the VOF model requirements, but it is suggested to keep it below 0.5 to clearly separate the two fluids. In the equation,  $u$  is the flow velocity,  $\Delta t$  is the time step, and  $\Delta h$  is the representative space discretization parameter.

$$Co = \frac{u \cdot \Delta t}{\Delta h} \quad (\text{Eq. 8})$$

- As found in STAR-CCM+ guide [21], the overset grid cells must move less than half the minimum cell size (in a second order temporal scheme) across two subsequent time steps, as larger movements could cause problems due to information exchange between the two regions. This condition is usually the most stringent.

In this case, the time step discretization is set to 0.02s. At the end of the pitch free decay base case simulation, the average of the Courant number is 1.40e-2, with a maximum value of 2.66e-1, so it is compliant with the reported suggested limit.

### **Volume of Fluid (VOF)**

As defined in Hirt and Nichols [45], the VOF method is a Eulerian numerical model to simulate the flows of various immiscible fluids in numerical grids, resolving the interface between different phases. At each time instant, the distribution of each phase is defined in terms of the volume fraction  $\alpha_i$  variable, defined in equation (9).  $V_i$  is the volume of phase  $i$  within the cell of volume  $V$ , so that when  $\alpha_i = 1$  the cell is full of phase  $i$ . The fluids within the cell are then treated as a mixture.

$$\alpha_i = \frac{V_i}{V} \quad (\text{Eq. 9})$$

This model has been selected as the literature review evidenced that it is the standard model in marine environment simulations in a RANS approach. In STAR-CCM+, the VOF model uses the Segregated Flow model, which individually solves each of the momentum equations.

### **Turbulence model, wall treatment, and $Y^+$**

The RANS approach needs to be closed with additional equations, which in turn require the introduction of new quantities. In this work, the  $k$ - $\epsilon$  approach has been selected as it conjugates robustness, accuracy, and computational cost. It is a two-equation model that introduces turbulent kinetic energy  $k$  and turbulent dissipation rate  $\epsilon$  and solves their corresponding transport equations. Even though some authors report the  $k$ - $\omega$  model or its variants to be more accurate, the  $k$ - $\epsilon$  model is reliable enough in the case of external flows when the wall gradients are not too strong [81], [82]. In this work, the Realizable Two-Layer  $k$ - $\epsilon$  model

from Shih et al. [83] has been selected, which uses a different transport equation for the turbulent dissipation rate. A specific characteristic of this option is the two-layer wall treatment that divides the boundary layer in two regions and allows for the application of the  $k$ - $\varepsilon$  model in the viscous-affected layer. The turbulent dissipation rate  $\varepsilon$  and the turbulent viscosity  $\mu_t$  are specified in the near-wall layer as a function of the wall distance and then blended smoothly with values obtained from the transport equation far from the wall. The wall distance (WD) solver can be frozen during the inner iterations, and this option will be tested in another paragraph.

The over-production of turbulence beneath surface waves in RANS models is a well-known problem originally brought to attention by Mayer and Madsen [84], and further assessed by Larsen and Fuhrman [85]. In particular, Larsen and Fuhrman proved that, among others, both the standard  $k$ - $\omega$  and  $k$ - $\varepsilon$  models are unconditionally unstable when used to model surface waves, causing an exponential growth of turbulent kinetic energy and eddy viscosity to appear. Therefore, they proposed new and formally stable closure models. Other authors approached the problem with a similar mindset: for example, Casalone et al. proposed the use of an upper bound for turbulent viscosity to limit its exponential growth [86]. As the authors report, this solution does not prevent the exponential growth phenomenon. Even though it can be used in the simulation of long phenomena without affecting the motion of a floating device, they recommend using it only when an accurate description of the generated turbulent field is not necessary and only if waves decay over time. In the reviewed literature, some authors chose new closure models based on the evidence brought by Larsen and Fuhrman, e.g. Wang et al. [69] adopted the  $k$ - $\omega$  SST-IDDES turbulence model from Gritskevich et al. [87]. In the present work, the only waves that affect the water surface are very small waves generated by the body motion. Therefore, the over-production problem has been tackled by introducing the Turbulent Viscosity User Scaling model and setting the Under-Relaxation Factor and the Maximum Ratio in the K-Epsilon Turbulent Viscosity solver to 0.9 and  $1e7$ , respectively. In this way, the growth of the turbulent viscosity is slowed down.

Turbulence models must also be selected according to the simulated problem characteristics, introducing the wall  $Y^+$  concept, also called non-dimensional wall distance. The selected two-layer approach is suitable for both low and high  $Y^+$  values, using the standard wall function and a blended wall function according to Reichardt's law [88], respectively. An ideal value of  $Y^+ = 1$  should be the target in order to correctly describe non-linear effects that would influence the damping coefficient estimation. As preliminary simulations highlighted, such a  $Y^+$  value would require a very small size of the near wall cells, which would then result in an

increased number of cells. The selected turbulence model is still robust enough to work with the characteristics of the mesh.

On top of the  $k$ - $\epsilon$  model, the Scale Resolving Hybrid (SRH) Turbulence model is included in this work, keeping the corresponding parameters  $\beta_\Psi$  and  $r_{dc}$  are left at their default levels. As reported in STAR-CCM+ guide, this model allows the user to “compute the subfilter scale eddy viscosity to provide closure to the time-averaged and spatially filtered Navier-Stokes equations” [21]. This model is included in order to try to improve the solution of turbulence quantities. STAR-CCM+ guide does not clarify whether the wall distance model is fit to work together with the SRH turbulence model but, as it works with both LES and RANS, it is considered to be a valid choice. A proper discussion on the effect of the inclusion of this model can be found later on in this paragraph.

### **Dynamic Fluid Body Interaction (DFBI)**

The Dynamic Fluid Body Interaction (DFBI) model is included in this work to simulate the motion of the floating body as the result of mechanical and multi-physics interactions. At each time step, STAR-CCM+ solves the governing equations of motion using the resultant force and moment on the body, thus updating its position and orientation. A Continuum Body type has been chosen so that the body can interact with the fluid, thus determining the forces and moments acting on it. A free motion is set on the body, but only the pitching motion (Y rotation) is activated. As a first option, the Maximum Number of Iterations in the 6-DOF solver is set to 5. Later in this chapter, the effect of increasing or decreasing the number of iterations available for the DFBI to solve the body motion will be investigated, while keeping fixed the maximum number of inner iterations.

### **Space and time discretization convergence studies and uncertainty analysis**

Since the simulation has been set up, it is possible to proceed with the verification step. Star-CCM+ is a commercial software, widely used for a variety of simulations, both in academia and the industry. This, however, does not guarantee that it is free of bugs and numerical errors. Therefore, it is crucial to check that the model is able to provide a unique solution to the set of partial differential equations (PDEs). In this work, instead of using a benchmark problem and then moving to the simulation of the FOWT platform, the verification process is reduced to the realization of a space and time discretization parameters convergence analysis, coupled with an uncertainty estimation on the results.

The most common technique to perform a convergence test is Richardson's Extrapolation (RE), which is suitable to test both the space parameter and the time step. As reported by Roache [72], RE was "first used by Richardson in 1910, and later embellished in 1927". The technique, also known as  $h^2$  extrapolation, assumes that the discrete solution  $f$  can be represented as a series expansion, shown in equation (10), where the  $g_i$  functions are independent from the discretization, whereas  $h$  is the discretization parameter. The classical application of RE method requires a second-order discretization method, so that  $g_1 = 0$ . In this case, two different numerical solutions  $f_1$  and  $f_2$  obtained with two discrete spacings  $h_1$  (fine grid) and  $h_2$  (coarse grid) are combined in equation (11) to estimate the exact solution  $f_{exact}$ , dropping higher order terms and including the refinement ratio  $r$  defined in equation (12).

$$f = f_{exact} + g_1 h + g_2 h^2 + g_3 h^3 + \dots \quad (\text{Eq. 10})$$

$$f_{exact} \cong f_1 + \frac{f_1 - f_2}{r^2 - 1} \quad (\text{Eq. 11})$$

$$r = \frac{h_2}{h_1} \quad (\text{Eq. 12})$$

A typical choice for the refinement is to double or halve the grid spacing, but it is not strictly required. At the same time, the convergence order is not necessarily 2, in which case it is suggested to use three different grid sizes to estimate the apparent or observed order of convergence  $p_{app}$  through equation (13). Roache already proposed a generalization of RE [72] to  $p$ -th order methods and  $r$ -value of the grid ratio, as in equation (14). Roache provides a fractional error estimator  $E_1$ , too, as in equations (15) and (16), and an actual fractional error  $A_1$ , as in equation (17).

$$p_{app} = \frac{\log\left(\left|\frac{f_{medium} - f_{coarse}}{f_{fine} - f_{medium}}\right|\right)}{\log(r)} \quad (\text{Eq. 13})$$

$$f_{exact} \cong f_1 + \frac{f_1 - f_2}{r^p - 1}$$

(Eq. 14)

$$E_{1, fine\ grid} = \frac{\epsilon}{r^p - 1}$$

(Eq. 15)

$$\epsilon = \frac{f_1 - f_{exact}}{f_{exact}}$$

(Eq. 16)

$$A_1 = \frac{f_1 - f_{exact}}{f_{exact}}$$

(Eq. 17)

However, Roache noticed that grid refinement studies were inconsistently reported in scientific literature, possibly leading to confusion and misinterpretation of the results [72]. This is why he introduced the Grid Convergence Index (GCI), to provide a uniform and reliable method to report and compare CFD studies. The author's idea was to provide a substitute for the  $\epsilon$  value obtained from equation (16) that could be used for any grid refinement study, using whatever values of  $p$  and  $r$ , relating it to the  $\epsilon$  that would be obtained from a grid refinement study with the same finest grid but using  $p = 2$  and  $r = 2$ . The equivalent  $\epsilon$  is in fact the GCI for the fine grid solution, expressed by equation (18), where  $\epsilon$  comes from equation (16). The author originally suggests using at least three grid solutions when the exact solution is not known, so that two different GCI values can be evaluated: from the fine grid to the intermediate grid ( $GCI_{12}$ ) and from the intermediate grid to the coarse grid ( $GCI_{23}$ ). These two values can be used to check whether the asymptotic range has been reached (which is a premise of both RE and GCI) by checking the approximate equivalence in equation (19).

$$GCI_{fine\ grid} = 3 \frac{|\epsilon|}{r^p - 1}$$

(Eq. 18)

$$GCI_{23} \cong r^p \cdot GCI_{12}$$

(Eq. 19)

Roache already found that the GCI can be used for non-cartesian and unstructured grids, if the refinement is systematic, and if it isn't, the method can be adapted using an effective value of  $r$  based on the number of cells in the domain. With reference to the nomenclature in equation (12), the effective refinement ratio can be evaluated using equation (20), which uses the exponent  $1/3$  as this work deals with a 3D case. This modification will come useful in this work, as not only the overset grid technique is used, but also the AMR method has been included, thus changing the grid look over time. It has to be noted that the GCI method is not perfect, e.g. Celik and Karatekin applied it to a non-uniform grid and they found that it tends to overestimate the uncertainty around the extrapolated value [89].

$$r_{eff} = \left( \frac{ncells_{fine}}{ncells_{coarse}} \right)^{1/3} \quad (\text{Eq. 20})$$

Reaching the asymptotic range to perform RE or to evaluate the GCI can be challenging as it might require extremely refined grids. In order to bypass this problem, Eça and Hoekstra proposed a new method for the estimation of the numerical uncertainty of CFD calculations based on refinement studies [73]. In particular, their technique first evaluates the error of any integral or local flow quantity  $\phi$  and then uses this value to estimate the numerical uncertainty. The process starts by computing the discriminating ratio  $R$  as in equation (21), to assess whether the solutions are converging. In particular the values of  $\phi$  are monotonically converging when  $0 < R < 1$ , which the authors prove to be equivalent to stating that  $p > 0$ . This is necessary as the error evaluation as a power series expansion is only possible for monotonically converging values, and most techniques such as RE show limitations in other cases like oscillatory convergence (see for example Celik et al. [90]).

$$R = \frac{\Phi_{fine} - \Phi_{medium}}{\Phi_{medium} - \Phi_{coarse}} \quad (\text{Eq. 21})$$

Provided that the condition on  $R$  is met, the authors propose four different error estimators, that can be seen in equations from (22) to (25). In particular, equations from (23) to (25) must be used when the error estimation with equation (22) is impossible or unreliable, i.e. when the observed convergence order is either too small or too large. In particular, equations (23) and (24) are meant for monotonically converging solutions, whereas the last one can even be used in case of non-monotonic convergence.

$$\epsilon_\phi \cong \delta_{RE} = \phi_i - \phi_0 = \alpha \cdot h_i^p \quad (\text{Eq. 22})$$

$$\epsilon_\phi \cong \delta_1 = \phi_i - \phi_0 = \alpha \cdot h_i \quad (\text{Eq. 23})$$

$$\epsilon_\phi \cong \delta_2 = \phi_i - \phi_0 = \alpha \cdot h_i^2 \quad (\text{Eq. 24})$$

$$\epsilon_\phi \cong \delta_{12} = \phi_i - \phi_0 = \alpha_1 \cdot h_i + \alpha_2 \cdot h_i^2 \quad (\text{Eq. 25})$$

Even though equations (22) and (25) require three grids, and equations (23) and (24) only require two grids, the authors recommend using at least four grids in order to make a quality check on the value of  $p$  when noisy data are expected. Using four grids also adds the possibility to evaluate  $\phi_0$  with a least-squares like method, i.e. by minimizing one of the functions in equations from (26) to (29) each associated to an error estimator in equations from (22) to (25).

$$S_{RE}(\phi_0, \alpha, p) = \sqrt{\sum_{i=1}^{n_g} (\phi_i - (\phi_0 + \alpha h_i^p))^2} \quad (\text{Eq. 26})$$

$$S_1(\phi_0, \alpha) = \sqrt{\sum_{i=1}^{n_g} (\phi_i - (\phi_0 + \alpha h_i))^2} \quad (\text{Eq. 27})$$

$$S_2(\phi_0, \alpha) = \sqrt{\sum_{i=1}^{n_g} (\phi_i - (\phi_0 + \alpha h_i^2))^2} \quad (\text{Eq. 28})$$

$$S_{12}(\phi_0, \alpha_1, \alpha_2) = \sqrt{\sum_{i=1}^{n_g} (\phi_i - (\phi_0 + \alpha_1 h_i + \alpha_2 h_i^2))^2}$$

(Eq. 29)

The authors also propose a modification of these equations, introducing a weighted approach that would privilege finer grids. Based on the discretization parameter, the weight  $w_i$  of each grid is defined in equation (30), and it leads to alternative error estimators, i.e. the objective is to minimize equations from (31) to (34).

$$w_i = \frac{\frac{1}{h_i}}{\sum_{i=1}^{n_g} \frac{1}{h_i}}$$

(Eq. 30)

$$S_{RE}^w(\phi_0, \alpha, p) = \sqrt{\sum_{i=1}^{n_g} w_i (\phi_i - (\phi_0 + \alpha h_i^p))^2}$$

(Eq. 31)

$$S_1^w(\phi_0, \alpha) = \sqrt{\sum_{i=1}^{n_g} w_i (\phi_i - (\phi_0 + \alpha h_i))^2}$$

(Eq. 32)

$$S_2^w(\phi_0, \alpha) = \sqrt{\sum_{i=1}^{n_g} w_i (\phi_i - (\phi_0 + \alpha h_i^2))^2}$$

(Eq. 33)

$$S_{12}^w(\phi_0, \alpha_1, \alpha_2) = \sqrt{\sum_{i=1}^{n_g} w_i (\phi_i - (\phi_0 + \alpha_1 h_i + \alpha_2 h_i^2))^2}$$

(Eq. 34)

The error estimation procedure begins by minimizing equations (26) and (31), primarily in order to estimate the observed order of convergence. Eça and Hoekstra provide information on the minimization process in an appendix to their work [73]. However, as the grid convergence study has been performed in MATLAB for this work [91], the built-in function *fminsearch* has been used to find the  $(\phi_0, \alpha, p)$  triplet that minimized each function. Other strategies have been tested, like the *fsolve* function, but they all failed due to numerical instabilities.

From the two estimated values of  $p$  from the non-weighted and weighted approaches in equations (26) and (31), the procedure can take multiple paths. If both values of  $p$  are negative, the behavior is considered anomalous and discarded. In this case, the numerical model must be revised. If only one of them is negative, the other one is taken as the best fit and the error is evaluated accordingly. If both of them are positive, a more in-depth investigation is required.

- For a theoretically 2<sup>nd</sup> order discretization method, if both the estimated values of  $p$  are between 0.5 and 2, then the estimated error is chosen according to which function (weighted or not weighted) yielded the lowest standard deviation.
- If  $p > 2$ , the original functions could produce small error estimates. In this case,  $\delta_1$  and  $\delta_2$  must be evaluated from the corresponding weighted and non-weighted functions, while  $\delta_{RE}$  is ignored. Then, the estimated error is chosen again according to which function was associated to the lowest standard deviation.
- If  $p < 0.5$ ,  $\delta_{RE}$  is too conservative, instead. Therefore, the procedure is similar to the  $p > 2$  case, but including  $\delta_{12}$  estimation as well, so that the error is chosen among six possibilities.

Once the discretization error  $\epsilon_\phi$  is obtained, together with the standard deviation  $\sigma$  of the fit and, in some cases, the convergence order  $p$ , it is possible to use it to evaluate the uncertainty  $U_\phi$  for each  $\phi_i$  value in the set. In particular, the standard deviation  $\sigma$  is compared to a *data range parameter*  $\Delta\phi$  defined in equation (35), defining two cases as in equations (36) and (37). In these equations, the safety factor  $F_s$  is set to 1.25 when  $0.5 \leq p \leq 2.1$ , i.e. when the error estimation is deemed reliable, and to 3 in all other cases. This method has the advantage of reducing to the GCI estimation for well-behaved data, i.e. monotonically convergent and smooth data from a 2<sup>nd</sup> order discretization method. In all cases where the error estimation technique could be criticized based on the data quality, e.g. when  $\sigma > \Delta\phi$ , the uncertainty estimation uses large safety factors, so that an approximative confidence range can be obtained even for poor quality results.

$$\Delta\phi = \frac{(\phi_i)_{max} - (\phi_i)_{min}}{n_{[g]} - 1} \quad (\text{Eq. 35})$$

$$\begin{cases} U_\phi(\phi_i) = F_s \epsilon_\phi(\phi_i) + \sigma + |\phi_i - \phi_{fit}| & \text{if } \sigma < \Delta\phi \\ U_\phi(\phi_i) = 3 \frac{\sigma}{\Delta\phi} (\epsilon_\phi(\phi_i) + \sigma + |\phi_i - \phi_{fit}|) & \text{if } \sigma \geq \Delta\phi \end{cases}$$

(Eqs. 36-37)

All the three proposed methodologies for error and uncertainty estimation are applied in this work to perform the grid convergence check. However, as Eça and Hoekstra do not explicitly refer to time discretization, the time step convergence study will only be based on RE and GCI methods.

The first oscillation peak amplitude is taken as the reference quantity  $\phi$ , similarly to previous studies [52], [53]. Common CFD simulations prefer using quantities that are more directly related to the flow characteristics, e.g. the friction factor for a fluid flow in a tube, but in this case it is difficult to identify a relevant parameter to describe the phenomenon other than the first oscillation peak. For example, the Reynolds number would not be significative in this case: first, because there is not a proper fluid flow around the structure; second, because it would be hard to identify the correct reference dimension for the problem to be used in Reynolds number estimation. Other dimensionless numbers have been found, like Keulegan-Carpenter number [92] or a new dimensionless number proposed by Balduzzi et al. for Darrieus turbines [93], but none of them seemed satisfactory for the scope of this work.

For the spatial grid convergence study, a ratio of 0.8 has been chosen between successive base sizes, as a compromise between a reasonable number of cells and a sufficient change from the finest grid to the coarsest one. In order to comply with Eça and Hoekstra recommendations, four grids have been tested, with a base size equal to 156m, 125m, 100m, and 80m, respectively. Moving to finer grids was not considered appropriate in this case, as the number of cells rapidly became too high, with about 15 million cells for a base size equal to 51m. Table [3] reports the number of cells and faces for each base size after the first iteration of the simulation, separated according to the region or boundary they belong to. These values already include the effect of the AMR. Another important consideration regards the time step value associated to each base size. Preliminary tests showed that keeping  $\Delta t$  fixed at 0.02s was not suitable for meshes finer than that of the base case, as it caused numerical divergence after the first seconds were simulated.

Therefore, the time step has been varied with a ratio of 0.8 between successive cases, in order to keep the Courant number constant and avoid divergence.

Table 3 – Number of cells and faces for different base sizes in the pitch free decay case.

<b>Base size</b>	<b>156</b>	<b>125</b>	<b>100</b>	<b>80</b>	<b>m</b>
<b>Tank cells</b>					
Tank	1.73E+06	2.73E+06	3.60E+06	5.68E+06	cells
Bottom boundary	7.80E+02	1.15E+03	4.50E+02	7.22E+02	faces
Inlet boundary	1.37E+03	1.85E+03	9.75E+02	1.33E+03	faces
Outlet boundary	1.37E+03	1.85E+03	9.75E+02	1.33E+03	faces
Side boundary	2.67E+03	3.70E+03	1.95E+03	2.66E+03	faces
Symmetry boundary	1.73E+04	2.32E+04	2.75E+04	3.59E+04	faces
Top boundary	7.55E+02	6.48E+02	7.53E+02	1.11E+03	faces
<b>Overset cells</b>					
Total	2.94E+05	4.63E+05	8.06E+05	1.34E+06	elements
<b>Total cells</b>	<b>2.05E+06</b>	<b>3.22E+06</b>	<b>4.44E+06</b>	<b>7.06E+06</b>	<b>elements</b>

The extrapolated value for the first oscillation peak from RE is  $6.12^\circ$ . Figure (7) shows the estimated error band obtained from RE and from different versions of the GCI method, applied to the three finest grids. In particular, the subscript “12” refers to the GCI applied to the fine and medium grid, while the subscript “23” refers to the GCI applied to the medium and coarse grid. Subscript “eff” refers to the use of the number of cells in the GCI process instead of the reference discretization parameter. A fair comparison can be made between RE and the two versions of  $GCI_{12}$ , as they are referred to the same grids. As expected, the GCI is more conservative, although the difference between the two is marginal. The  $GCI_{23}$  results have been used to prove that the asymptotic range has been reached, as the approximate equivalence in equation (19) yields  $0.2265 \cong 0.2263$ . It is important to notice that the observed order of convergence is close to 5 when estimated using the reference space discretization parameter, and close to 7 when the number of cells is used. However, no clear explanation has been found for this behavior.

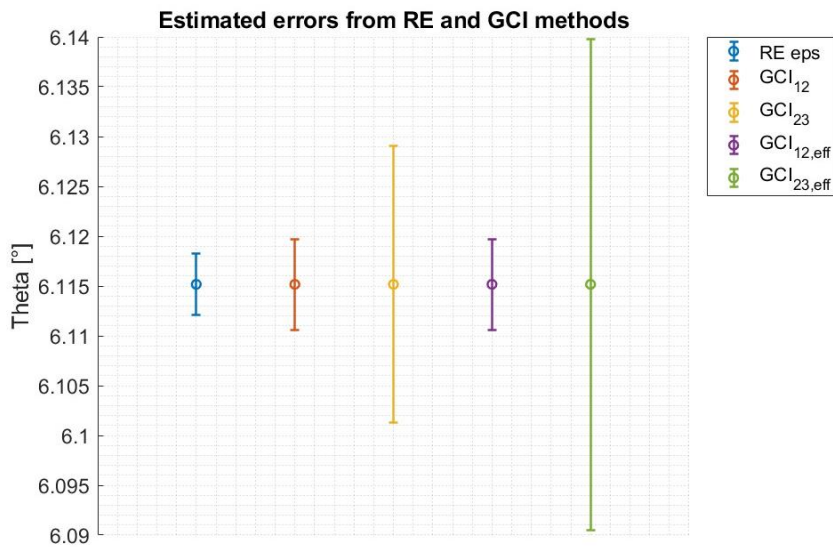


Figure 7 - Estimated errors for the first pitch oscillation peak from RE and GCI methods for the grid discretization parameter.

Figure (8) shows the results of the method from Eça and Hoekstra instead. The dotted line represents the extrapolated value for the first oscillation peak, while the blue line connects the results of each grid, and the error bars are obtained from the evaluated uncertainties for each grid. The new extrapolated value is equal to  $6.14^\circ$ , which is close enough to the one obtained from RE. As the figure shows, all grids provide an underestimation of the extrapolated value, but the latter still falls within the uncertainty range. From this analysis, the optimal base size would be 100m, as it seems to provide an acceptable uncertainty range, without refining the grid too much. Although the computational time would be reduced using coarser grids, as shown in table [4], their uncertainty range is too large, and it probably indicates a lower quality of the results.

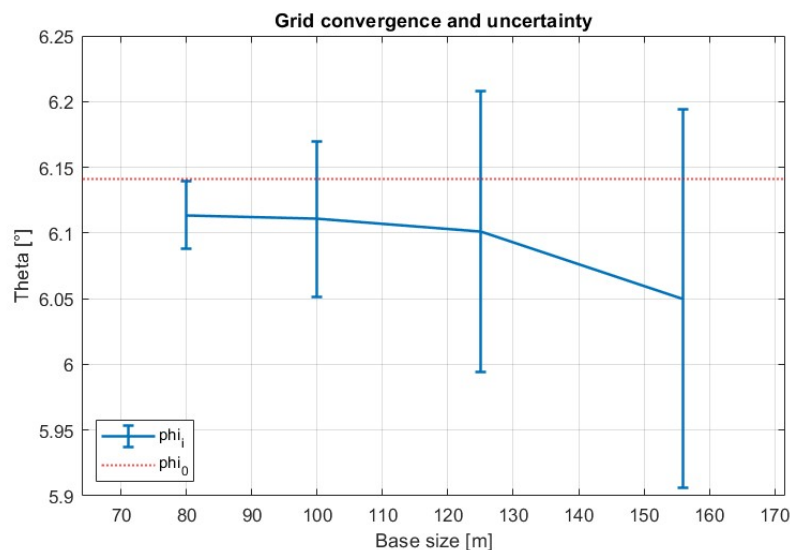


Figure 8 - Grid convergence trend and uncertainty ranges for the pitch motion.

Table 4 - Computational time comparison between different base sizes.

Base size	80	100	125	156	m
<b>Solver CPU time per time step</b>	6114.2	3134.79	2513.31	1545.7	s
<b>Solver elapsed time per time step</b>	39.38	20.02	15.87	9.92	s
<b>Solver iteration CPU time</b>	176.24	69.39	64.96	34.81	s
<b>Solver iteration elapsed time</b>	1.1	0.43	0.41	0.22	s
<b>Total solver CPU time</b>	6568.56	3055.89	2060.85	1439.46	h
<b>Total solver elapsed time</b>	41.22	19.18	12.93	9.03	h

After completing the convergence study with reference to the mesh cell size, it is necessary to perform a time step convergence study. The ratio between subsequent values of the discretization parameter is still 0.8, in order to use time steps values that are comparable to those used for the previous convergence study, while the base size is kept fixed at 100m. The reference value is still the first pitch oscillation peak amplitude, and the extrapolated value from RE is  $6.08^\circ$ , which is slightly lower than the result obtained from the previous study. While this result still falls within the previously obtained uncertainty range, the error bars obtained here are too small to contain either of the extrapolated values from the grid convergence study, as seen in figure (9). Figure (10) shows the solution trend according to the time step size compared to the extrapolated values, apparently highlighting a significant drop when the time step is lower than 0.02s. A closer inspection shows, however, that the values are extremely close to each other. So, it is possible to compare the computational time in order to decide whether the accuracy gain is worth the computational time increase. As it can be seen from table [5], reducing the time step from 0.02s to 0.016s corresponds to approximately 2.5 extra hours, which is considered too much compared to the original time (also called *Total solver elapsed time*) required to complete the simulation. Therefore, 0.02s is assumed to be the optimal time step in this case.

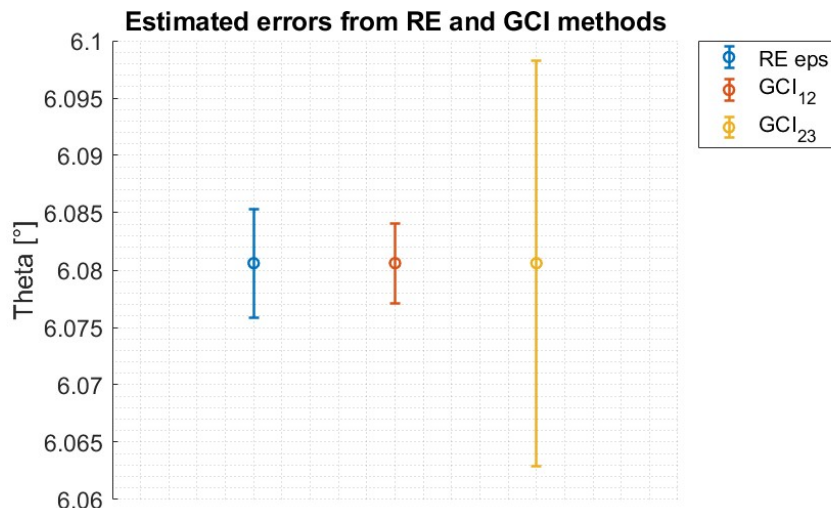


Figure 9 - Estimated errors for the pitch motion using RE and GCI methods for the time step.

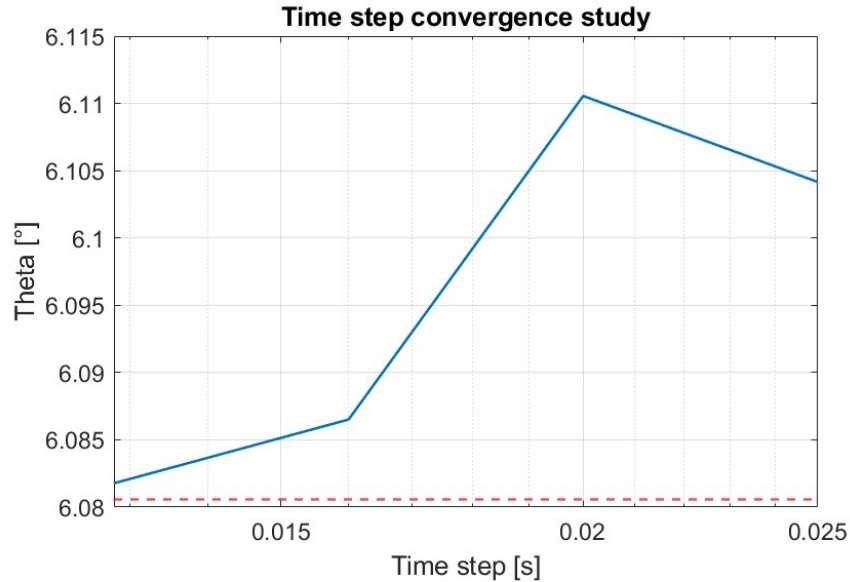


Figure 10 - Time step convergence trend for the pitch motion.

Table 5 - Computational time comparison between different time steps.

Time step	2.50E-02	2.00E-02	1.60E-02	1.28E-02	s
<b>Solver CPU time per time step</b>	2846.65	3134.79	3151.17	2972.39	s
<b>Solver elapsed time per time step</b>	18.05	20.02	20.53	19.65	s
<b>Solver iteration CPU time</b>	66.78	69.39	71.93	69.12	s
<b>Solver iteration elapsed time</b>	0.42	0.43	0.45	0.43	s
<b>Total solver CPU time</b>	2200.26	3055.89	3447.58	4326.85	h
<b>Total solver elapsed time</b>	13.81	19.18	21.63	27.15	h

### Comparison between different simulation setups

Using the optimal grid base size and time step, it is possible to independently check some of the most relevant solvers and their corresponding options included in the simulation. This investigation is important to assess whether it is possible to improve the simulation in terms of computational time, without compromising the accuracy of the results. In this section various tests will be performed: first, the SRH model is removed; then, the number of iterations for the DFBI solver will be varied; finally, the wall distance solver will be frozen.

Turbulence modelling is an important part of this study, as evaluating damping coefficients that take into account non-linear effects requires an accurate solution of the boundary layer, where phenomena like viscous stresses and vortex shedding can occur. While the choice between closure models like the k- $\epsilon$  model and the k- $\omega$  model has already been justified through the results found in the literature, no relevant results have been found regarding the SRH model use for floating structures. Therefore, a comparison between the results obtained with and without this model is performed. The first and most evident effect of removing this solver is the

reduction of the computational time from approximately 19h, to just over 17h. From figure (11), it can be seen that the kinematics of the platform do not seem to vary, e.g. the first oscillation peak reaches 6.0917 when the SRH is removed, compared to the value of 6.0869 obtained in the base case, and the peak is reached in the same time instant. Similarly, the moment around the y axis is almost identical in the two cases, even though the figures have been omitted in this work for simplicity. However, a clear drawback is found in the large increase of all turbulent quantities, as seen in figures from (12) to (15) that represent their average value in relevant regions of the domain. The average values have been selected to perform the comparison rather than the maxima as the latter did not provide useful insights. Maximum values of turbulent quantities can reach very high values, some order of magnitude larger than the corresponding average values, and they oscillate without a clear pattern. Therefore, it is likely that instantaneous maximum values are the result of local anomalies in the numerical solution, that do not significantly affect the overall behavior of the platform. A more in-depth investigation could be performed in the future to verify where maximum values can be found in the grid, as it could suggest how to improve the grid refinement strategy or which turbulence model to choose.

Figures from (12) to (15) show that, without the SRH model, all turbulent quantities keep growing for about the first two oscillations and they become almost one order of magnitude larger than in the case with the SRH model. In the literature, no relevant data have been found on turbulence quantities evaluation during the free decay motion of a floating platform. The most similar problem is the exponential generation of numerical turbulence beneath surface waves (see for example [85], [86]). The observed behavior in figures from (12) to (15) reminds the numerical turbulence generation and propagation found by Casalone et al. when wave propagation was tested in the presence of a body at the water-air interface [86]. Future studies on turbulence generation and propagation through the domain would be needed, for example to compare data to experimental results and to check whether the overset grid can be considered a numerical turbulence source. Nonetheless, the SRH model is considered necessary in this work to correctly complete the simulation and it will be included in all the next simulations.

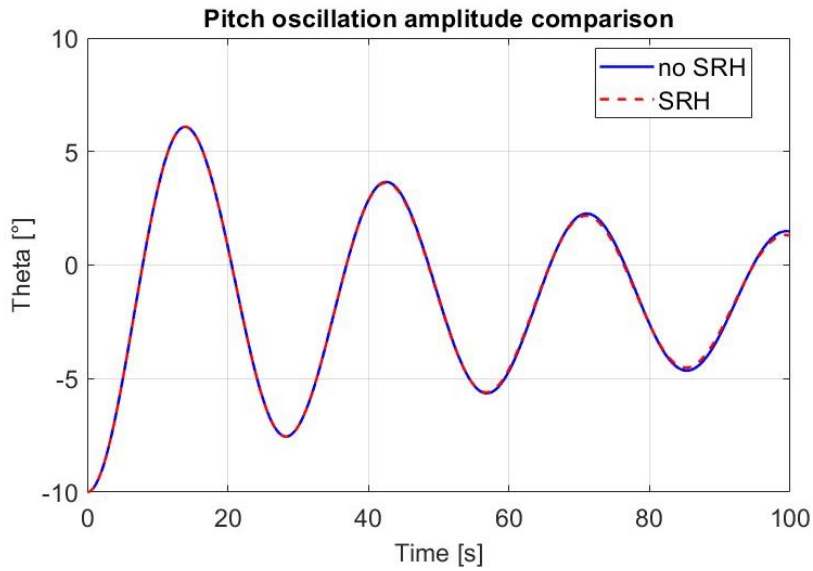


Figure 11 - Pitch orientation plot comparison between the case with and without the SRH model.

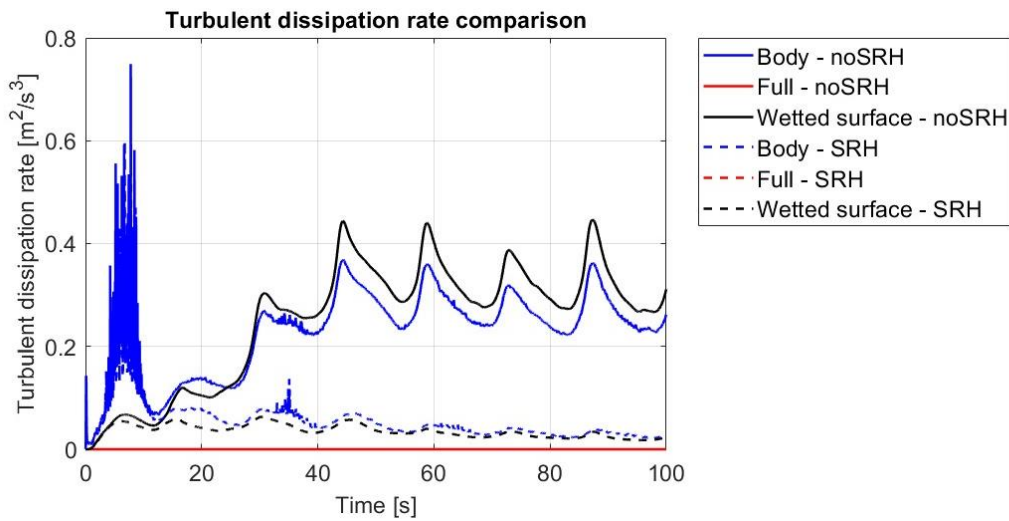


Figure 12 - Turbulent dissipation rate plot comparison between the case with and without the SRH model.

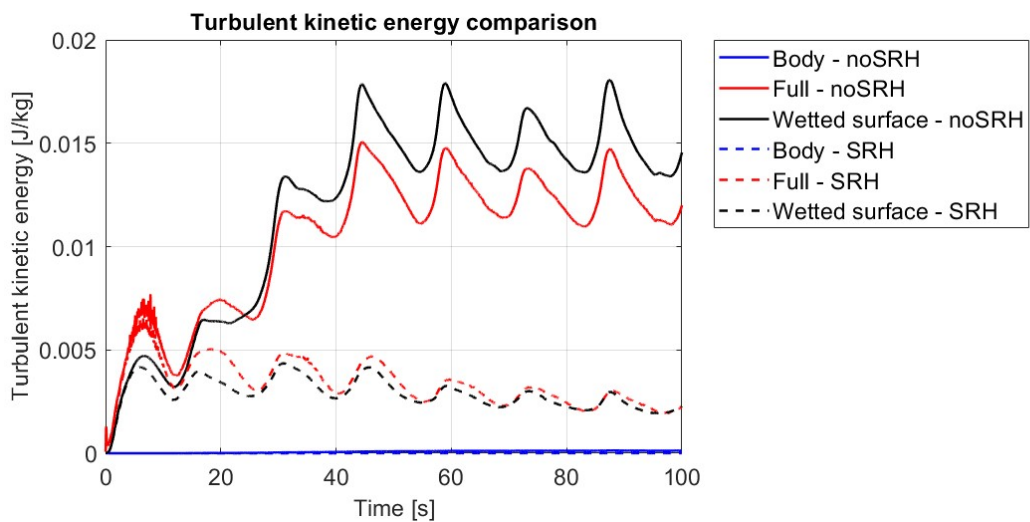


Figure 13 - Turbulent kinetic energy plot comparison between the case with and without the SRH model.

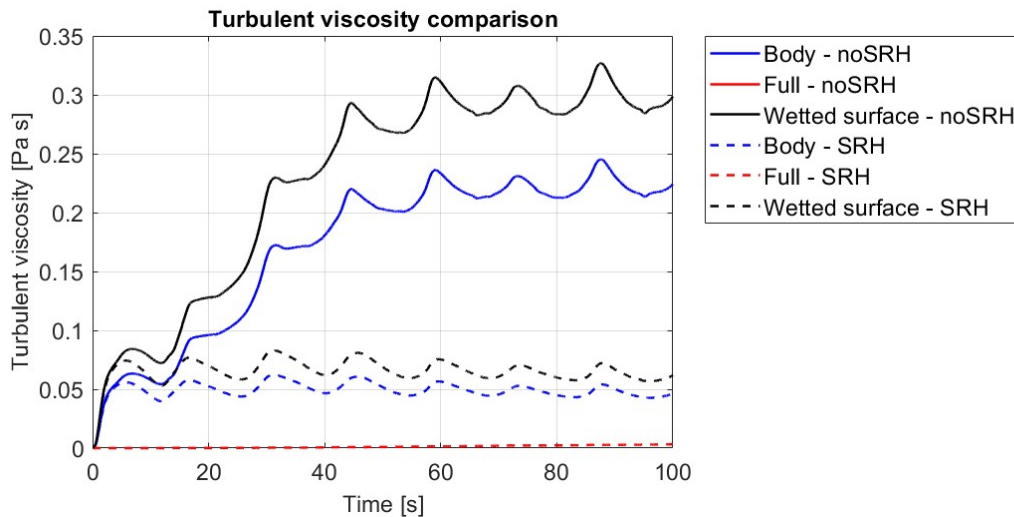


Figure 14 - Turbulent viscosity plot comparison between the case with and without the SRH model.

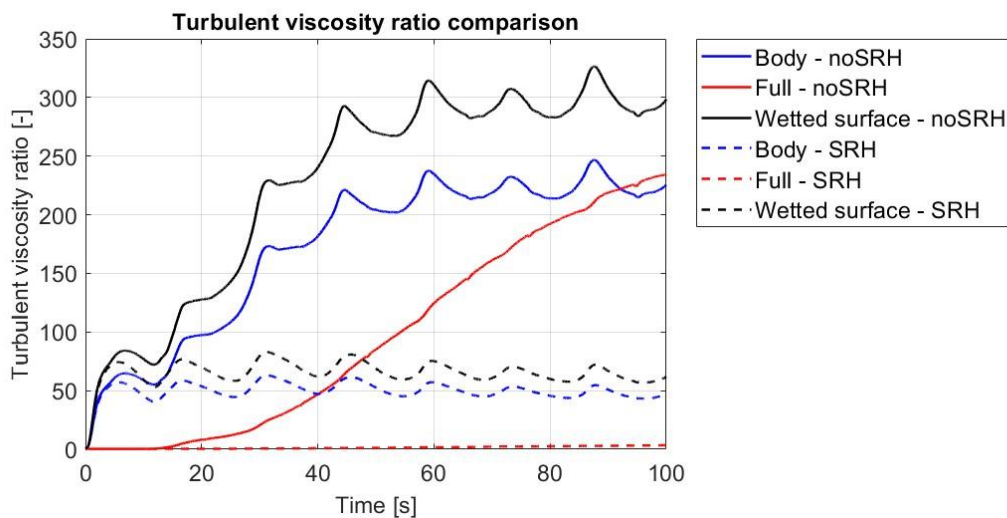


Figure 15 - Turbulent viscosity ratio plot comparison between the case with and without the SRH model.

The next test involves the possibility to freeze the Wall Distance (WD) solver. This option has been tested with the objective of reducing the computational time, by removing some calculations. However, the computational time unexpectedly increased by almost 1.5h compared to the base case, as seen in table [6]. This result has been attributed to the fact that not updating the solver leads to lower quality results that slow down the convergence on all other flow quantities. Both the pitch oscillation amplitude, shown in figure (16), and the moment around the y axis plots show little differences compared to the base case, suggesting that the increase in computational time does not correspond to an improvement in the quality of the solution. The WD solver evaluates the wall distance parameter  $d$  for the relevant turbulent quantities and wall treatment methods. However, freezing it produces negligible changes in the plots of the average and maximum values of turbulent quantities over time. Since freezing this solver only slows

down the simulation without increasing the quality of the results, it will not be frozen in the following simulations.

Table 6 - Computational time comparison with and without freezing the WD solver.

	Base case	WD frozen	
<b>Solver CPU time per time step</b>	3134.79	3058.79	s
<b>Solver elapsed time per time step</b>	2.00	19.35	s
<b>Solver iteration CPU time</b>	69.39	70.67	s
<b>Solver iteration elapsed time</b>	0.43	0.44	s
<b>Total solver CPU time</b>	3055.89	2764.43	h
<b>Total solver elapsed time</b>	19.18	20.56	h

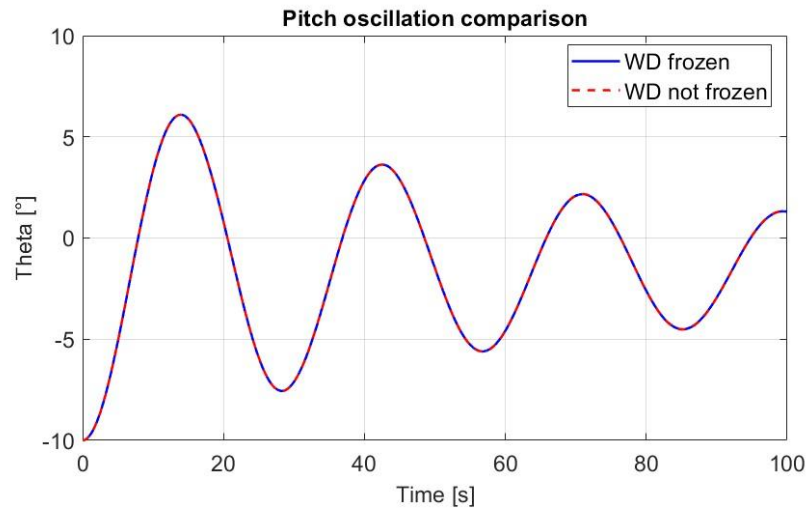


Figure 16 - Pitch oscillation amplitude comparison with and without freezing the WD solver.

Another test involves changing the number of iterations of the DFBI solver. In particular, two possibilities are explored, compared to the base case where the solver is allowed to perform up to five iterations: reducing the maximum allowed iterations to one to reduce the computational time or increasing it to ten to improve the quality of the results. It is important to notice that with ten iterations, the last ones are performed after the inner iterations of the code and therefore they can be seen as refinements on the DFBI solution. The pitch oscillation amplitude plots do not significantly differ as shown in figure (17), but the computational time is largely reduced. As it can be seen from table [7], choosing to perform only one iteration significantly cuts the computational time by more than 40%. Comparing the turbulent quantities behavior, all three cases perform similarly, with some negligible differences around the last oscillation. Some more noticeable differences can be seen in figures (18) and (19), that show the wave height 80m in front and 80m behind the platform vertical axis over time. In particular, the

measurement has been taken for a point 10cm far from the symmetry plane in the y direction. It can be seen that numerical imperfections accumulate, making waves look different near the end of the simulations. However, the waves are around 2/3cm high, so they are negligible when studying a 35m high body that could experience 2m high or more waves during operation. Overall, the optimal maximum number of iterations is one, as it produces acceptable results with the lowest computational time.

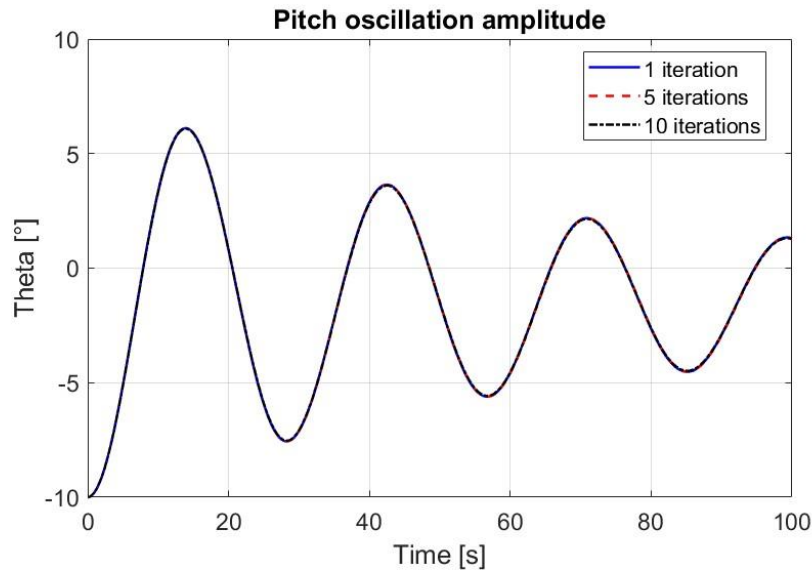


Figure 17 - Pitch oscillation amplitude comparison between the three tested cases with different maximum numbers of DFBI iterations.

Table 7 - Computational time comparison between the three tested cases with different maximum numbers of DFBI iterations.

	<b>1 iteration</b>	<b>5 iterations</b>	<b>10 iterations</b>	
<b>Solver CPU time per time step</b>	2859.84	3134.79	3935.22	s
<b>Solver elapsed time per time step</b>	18.47	20.02	25.02	s
<b>Solver iteration CPU time</b>	110.69	69.39	278.04	s
<b>Solver iteration elapsed time</b>	0.69	0.43	1.74	s
<b>Total solver CPU time</b>	1768.37	3055.89	3683.49	h
<b>Total solver elapsed time</b>	11.10	19.18	23.11	h

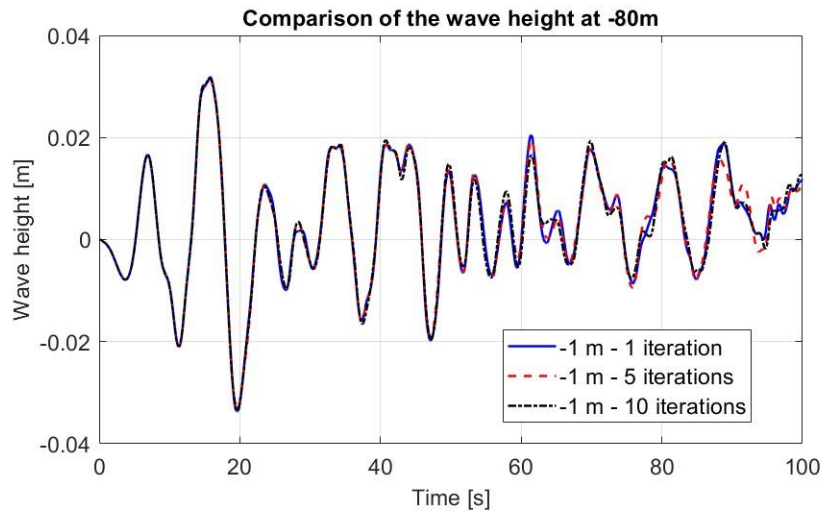


Figure 18 - Wave height comparison 80m behind the platform axis.

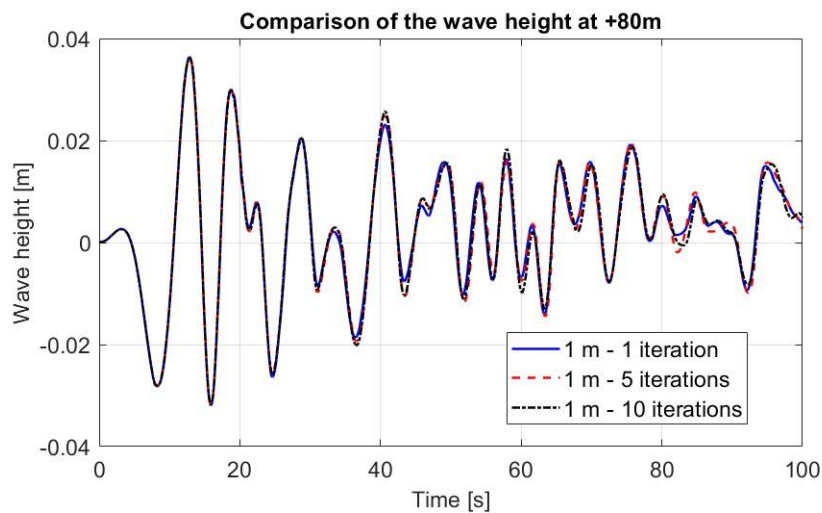


Figure 19 - Wave height comparison 80m in front of the platform axis.

### Heave free decay

Once the pitch free decay simulation has been successfully concluded and the most relevant solver options have been studied, the easiest path would be to replicate the same setup to perform the heave free decay simulation. However, as it will be clearer from the next sections, this is not possible, and therefore an *ad hoc* investigation is mandatory. In particular, the next sections will focus on what changes from the pitch free decay simulation setup to the heave free decay one. All omitted details should be considered identical to how they were set in the previous simulation.

## **Simulation setup**

A first and fundamental difference between the pitch and the heave free decay simulations is the computational domain. In the heave free decay case, the platform is initially aligned with the vertical axis, but it starts 12m below the equilibrium condition. Therefore, the refinement region around the platform must be taller in order to accommodate the positive oscillation peaks. A preliminary simulation including this consideration showed, however, that the original refinement region was not suitable for the heave free decay case as it generated a massive amount of cells that the solver was not able to manage.

Therefore, significant changes in how the mesh is created have been done. The reference size  $\lambda$  and the reference height  $h$  have been reduced to 64m and 1m, respectively. As the proportionality between  $\lambda$  and the tank edges lengths did not change, the tank is now smaller: it is 384m long, and 192m wide, while the tank height and the water depth did not change. In an attempt to further reduce the number of cells, the number of cells per height has been reduced from 16 to 12, making them slightly larger. Since the pitch free decay investigation revealed that the generated waves were very small, the refinement regions across the water free surface are thinner: the smaller disc has a total height of  $0.6 h$  (60cm), while the larger disc has a total height of  $1.6 h$  (160cm). The refinement region that had been created to smoothly transition towards larger cells, now extends above the SWL for  $1.5 h$  (1.5m). However, the most evident change to the spatial grid regards the cells that are closer to the floating platform. The refinement region around it has been significantly modified and it is made of small cylindrical regions around the platform's tower on top of a larger cylindrical base. The base cylinder is 30m high and its bottom face is 34m below the SWL, while the smaller cylinders on top of it reach 25m above the SWL. The base cylinder has a 70m radius, while the smaller ones have a 7.5m radius. This region has been built so that it accommodates the platform motion cutting refined cells in the air portion of the domain, where an accurate description of the fluid flow is not required. Finally, some more cells have been cut by removing the prism layer from the overset region just for the upper faces of the platform's towers. A side view of the mesh on the symmetry plane can be seen in figure (20), while a top view of the mesh at the SWL can be seen in figure (21). Figures (22) and (23) report details from the previous views of the mesh, to highlight the overset mesh.

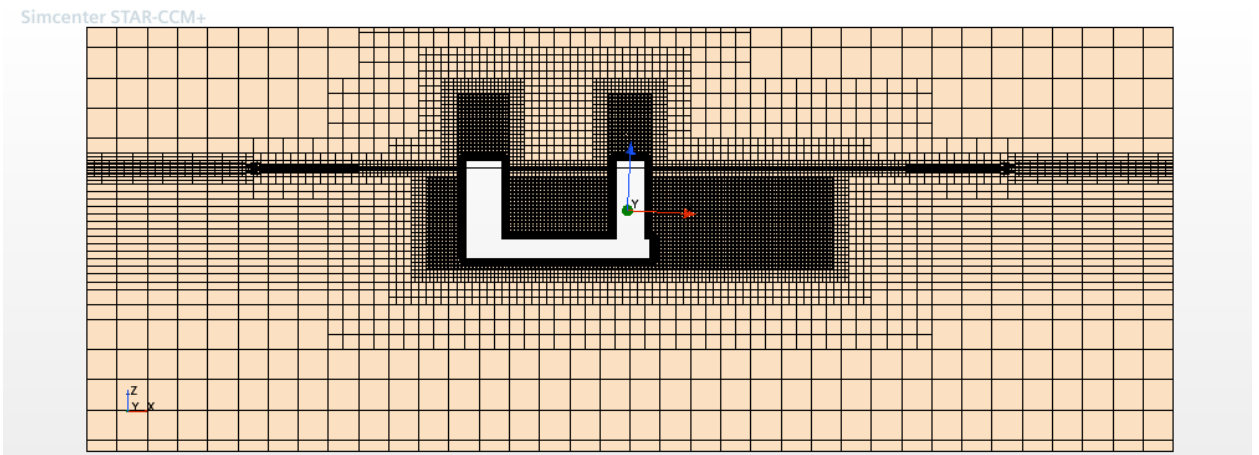


Figure 20 - Side view of the generated mesh for the heave free decay tests.

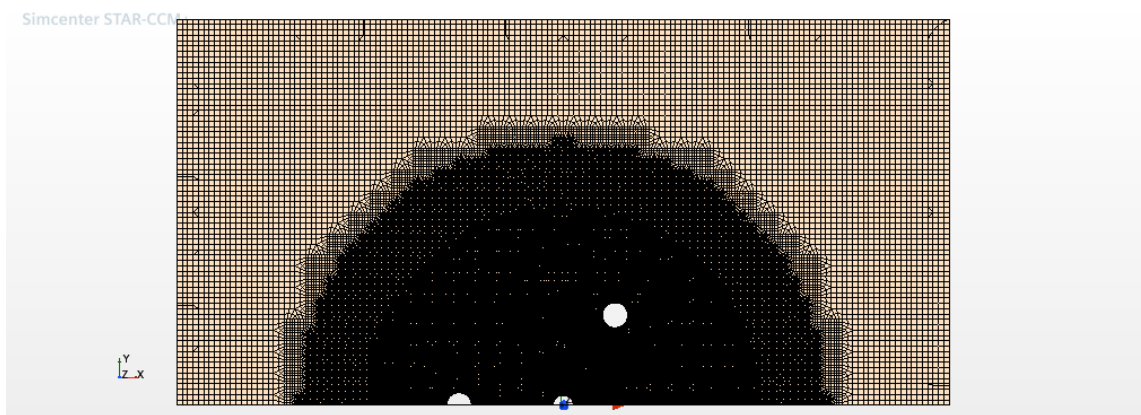


Figure 21 - Top view of the generated mesh for the heave free decay tests.

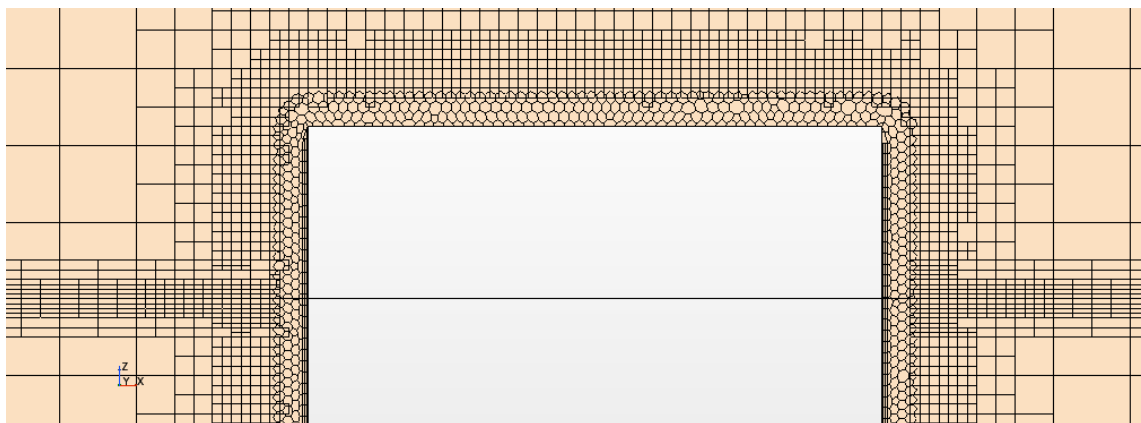


Figure 22 - Side view detail of the generated mesh for the heave free decay tests.

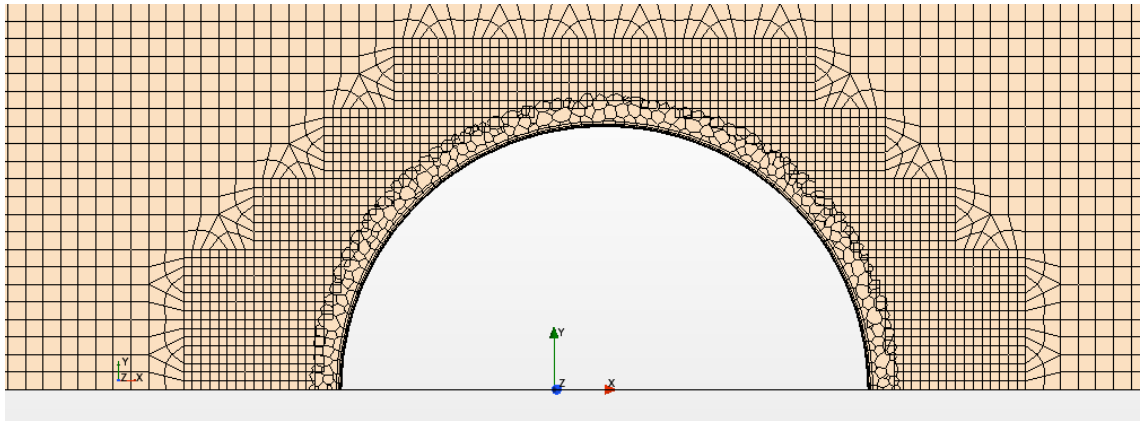


Figure 23 - Top view detail of the generated mesh for the heave free decay tests.

The modified mesh was not enough to successfully run the simulation, as other preliminary tests suggested that the time step should have been largely reduced in order to prevent the simulation from diverging, likely increasing the computational time by a lot. The problem has been solved instead by increasing the maximum number of iterations for the DFBI's 6-DOF solver back to 5, while keeping the time step at 0.02s. No other models or options have been modified.

### **Space and time discretization convergence studies and uncertainty analysis**

After the necessary modifications, the simulation setup was suitable to run the convergence studies for all values of the discretization parameters. The same methods that have been explained for the pitch free decay case have been used here. The ratio between successive base sizes (space discretization parameters) and successive time steps is again set to 0.8 and during the grid convergence study the time step is changed according to the base size in order to keep the Courant number fixed. Finally, the reference quantity in both convergence studies is the first oscillation peak amplitude.

The grid convergence study revealed that the simulation using a base size of 80m for the spatial grid led to unexpected results. While the oscillation amplitude plot is similar to that of other cases, as seen in figure (24), the apparent order of convergence is negative when this simulation is accounted for. In other words, the series of oscillation peak amplitudes obtained with different base sizes is diverging. Ignoring this simulation, however, the apparent order of convergence is equal to 4.26 when the base sizes are used, and to 7.42 when the number of cells is used. These results are closer to those obtained for the pitch free decay. Although an in-depth investigation would be required in order to explain the behavior of the simulation with a base size equal to 80m, time constraints led to the decision of just using the other three simulations. In

fact, different explanations to this behavior have been tested, such as the fact that the Courant number could have been inadequate, but none of them led to the solution to the problem, e.g. the average Courant number at the end of the simulation with a base size equal to 80m is  $1.22e-2$ . At the same time, neither reducing the ratio between successive discretization parameters nor increasing it above the coarsest case have been deemed reasonable solutions. The first option would make subsequent grids too similar to each other, so that the extrapolation procedure would be inaccurate. The second option has been discarded because the simulation with a base size of 156m already produced lower quality results. As it can be seen from figure (24), a coarse grid causes numerical imperfections to accumulate and the overall behavior of the platform is influenced, suggesting that coarser grids would not correctly capture the phenomenon. Unfortunately, using three grids prevents the application of Eça and Hoekstra's method for the uncertainty estimation [73]. Therefore, figure (25) reports the error estimation from RE and the GCI method, including the results obtained using the number of cells. The extrapolated value of the first oscillation peak amplitude is 7.00m, but the accuracy of the results is lower than in the pitch case as proven by the larger error bars. In fact, the value of  $\epsilon$  from the RE is 0.0133, while  $GCI_{12}$  is equal to 2.51. The  $GCI_{23}$  results have again been used to prove that the asymptotic range has been reached, as the approximate equivalence in equation (19) yields  $6.4790 \cong 6.4921$ . Therefore, even though the accuracy is lower, the results can still be trusted from a verification point of view. In this case, a base size equal to 100m has been chosen among the three simulations that are considered valid, as it minimizes the error compared to the extrapolated solution as shown in figure (26), where the solution for each base size is compared to the extrapolated value. Even though the computational time is significantly higher than the ones of coarser grids, as shown in table [8], this has been considered a minor inconvenience compared to the loss of accuracy.

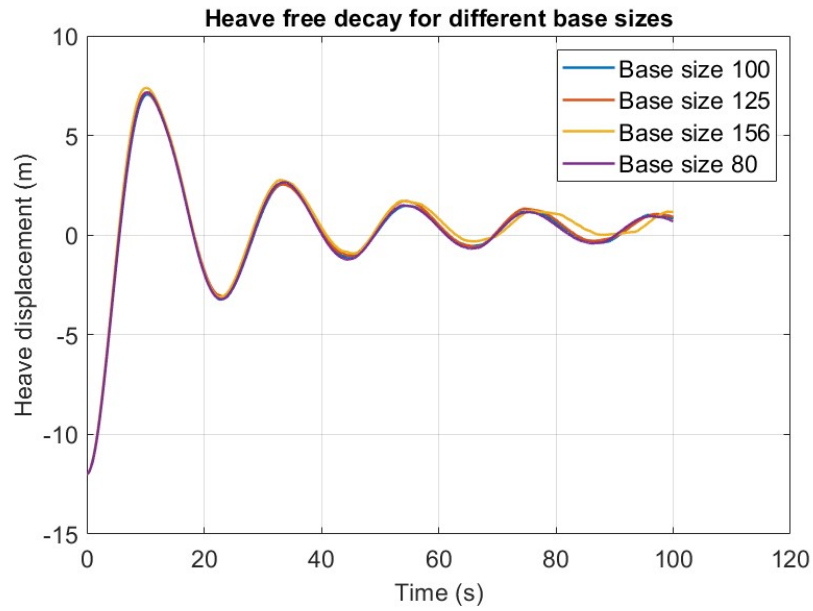


Figure 24 - Comparison of heave free decay oscillation amplitude for different spatial grid base sizes.

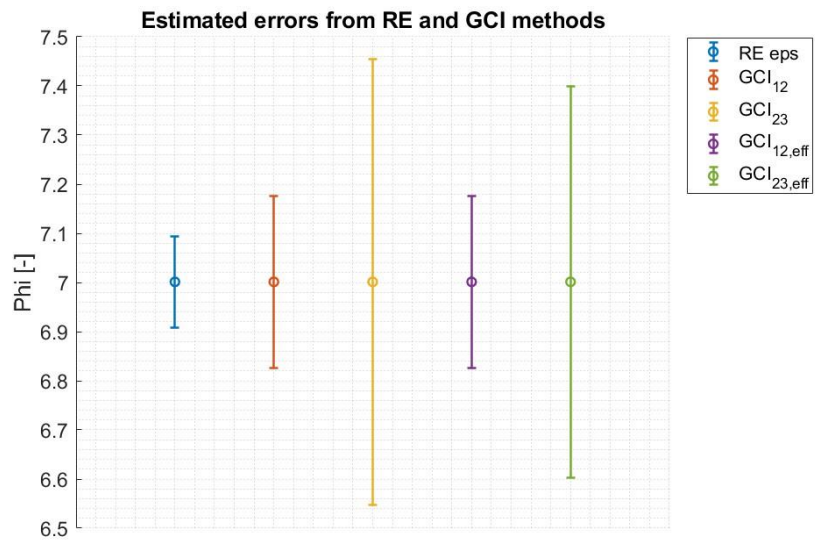


Figure 25 - Estimated errors for the first heave oscillation peak using RE and GCI methods for the grid discretization parameter.

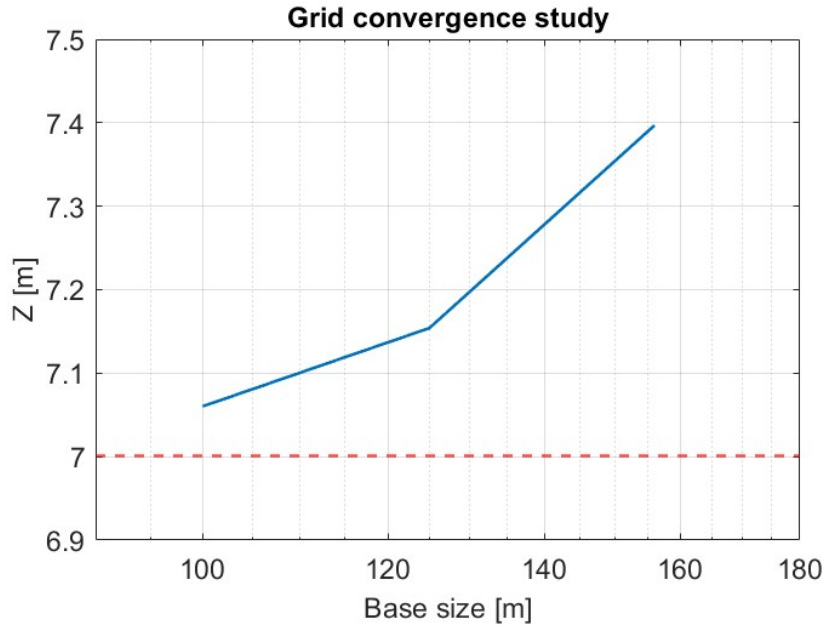


Figure 26 - Convergence study trend for different base sizes.

Table 8 - Computational times comparison between different base sizes.

Base size	80	100	125	156	m
<b>Solver CPU time per time step</b>	6872.32	4915.59	5084.28	2246.42	s
<b>Solver elapsed time per time step</b>	43.6	31.07	32.24	14.21	s
<b>Solver iteration CPU time</b>	170.06	115.6	110.31	52.65	s
<b>Solver iteration elapsed time</b>	1.07	0.72	0.69	0.33	s
<b>Total solver CPU time</b>	8700.41	4629.13	2677.06	1326.28	h
<b>Total solver elapsed time</b>	54.58	29.04	16.8	8.32	h

In order to complete the verification process for the heave free decay, the time step convergence study has been performed. The same time steps that had been selected for the pitch free decay case are tested here, while keeping the value of the base size constant. Figure (27) reports the estimated errors from RE and the GCI method. It can be seen that the error bar obtained from the GCI method ( $GCI_{12} = 0.049$ ) for the finest grids is smaller than the one obtained from RE ( $\epsilon = 0.001$ ), even though they are still considerably small. As the GCI method is generally considered to be more conservative, this result was unexpected. However, figure (28) shows that the first oscillation peak amplitude values rapidly reach the asymptotic region, so that a high confidence level is expected. A time step equal to 0.02s has been selected for future calculations as it is the best compromise between the accuracy in the results, and the computational time. As table [9] shows, the computational time is significantly larger than in the pitch free decay case, especially for smaller time steps.

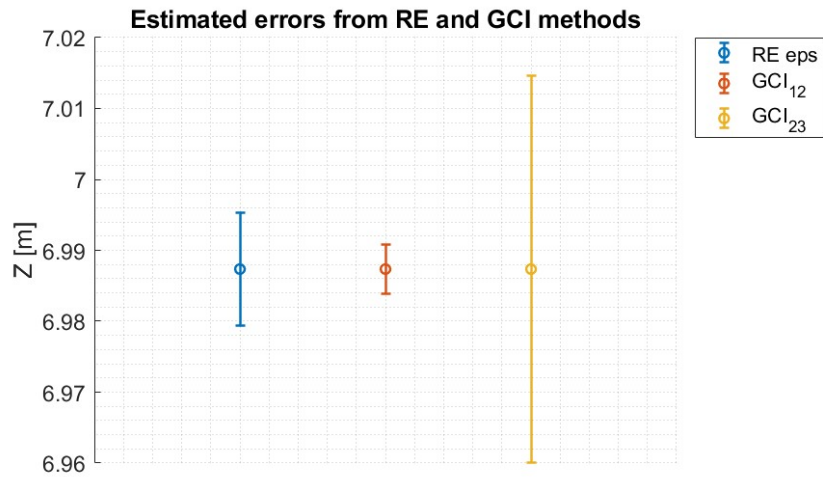


Figure 27 - Estimated errors for the heave free decay case evaluated with RE and with the GCI method.

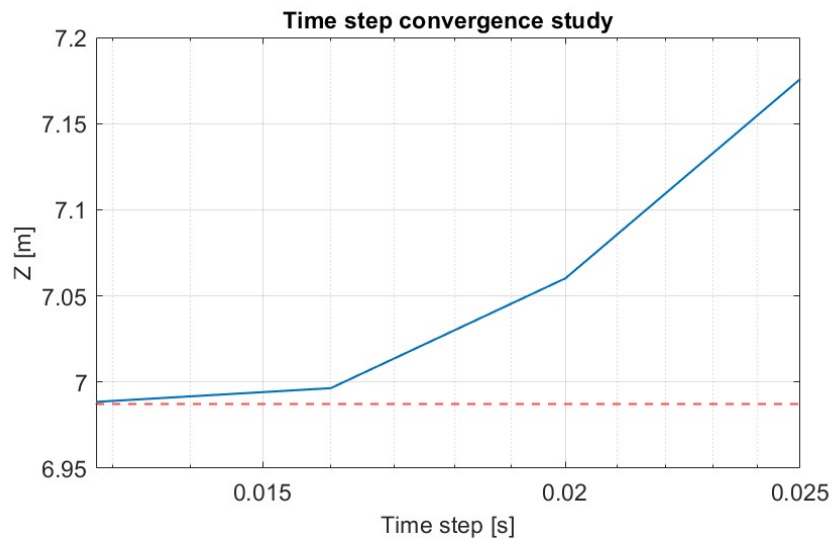


Figure 28 - Heave first oscillation peak for different time steps compared to the extrapolated value from RE.

Table 9 – Computational time for the heave free decay simulation with different time steps.

Time step	2.50E-02	2.00E-02	1.60E-02	1.28E-02	s
<b>Solver CPU time per time step</b>	5782.2	4915.59	5744.92	7780.48	s
<b>Solver elapsed time per time step</b>	36.87	31.073	36.51	49.2212	s
<b>Solver iteration CPU time</b>	151.9	115.6	97.53	136.87	s
<b>Solver iteration elapsed time</b>	0.95	0.7239	0.6112	0.858	s
<b>Total solver CPU time</b>	4140.02	4629.13	5084.48	8143.44	h
<b>Total solver elapsed time</b>	25.92	29.04	31.9	51.1	h

## Results and post-processing

The free decay simulation tests that have been run in the previous chapter were necessary in order to find a proper setup to accurately simulate the platform motion with the objective of post-processing the results to obtain relevant descriptive parameters. In particular, this work is the result of the collaboration with MORE Lab at Politecnico di Torino and this chapter is the result of the application of the method proposed by Casalone et al. for the identification of viscous damping parameters [80]. Even though the original paper refers to wave energy converters, the theory behind the proposed method is generally valid for floating structures. The essential premises and equations are reported, but it is advised to refer to the original publication for a detailed explanation.

Starting from Cummins' equation [94] and with reference to the pitch motion, the authors reached the non-dimensional linear equation of motion in the canonical form expressed by equation (38). In this equation  $\delta$  is the pitch angle,  $\omega_\delta$  is the damped natural pitch frequency, and  $\alpha_{eq}$  is expressed by equation (39), where  $\alpha$  and  $\beta$  are the linear and quadratic extinction coefficients, respectively.

$$\ddot{\delta} + 2\alpha_{eq}\dot{\delta} + \omega_\delta^2\delta = 0 \quad (\text{Eq. 38})$$

$$\alpha_{eq} = \alpha + \frac{4}{3\pi} \omega_\delta \delta_i \beta \quad (\text{Eq. 39})$$

The coefficients  $\alpha$  and  $\beta$  are linked to the linear dissipation coefficient  $B_{55,1}$  and the quadratic dissipation coefficient  $B_{55,2}$  by equations (40) and (41), respectively. The subscript 55 refers to the pitch motion, while  $I_{55}$  is the moment of inertia and  $A(\omega_\delta)$  is the added mass term evaluated at the natural frequency of the system.

$$\alpha = \frac{B_{55,1}}{2(I_{55} + A(\omega_\delta))} \quad (\text{Eq. 40})$$

$$\beta = \frac{B_{55,2}}{(I_{55} + A(\omega_\delta))} \quad (\text{Eq. 41})$$

Obtaining a reliable estimation of the coefficients  $B_{55,1}$  and  $B_{55,2}$  is the final objective of this chapter, as well as the corresponding parameters for the heave motion. In order to do so, it is assumed that equation (38), that represents a linear underdamped system, can be associated to the envelope curve of a decay starting from  $\delta_0$ , defined in equation (42). When equation (42) is applied to two consecutive peaks  $i$  and  $i + 1$  of the decay curve, a logarithmic decay is evaluated and the linear extinction coefficient  $\alpha_{eq}$  is evaluated by means of equations (43) and (44). The computation also requires the evaluation of the damped pitch frequency by means of equation (45).

$$\delta = \delta_0 e^{\alpha_{eq} t} \quad (\text{Eq. 42})$$

$$\alpha_{eq} = \frac{1}{t_{i+1} - t_i} \ln \left( \frac{|\delta_i|}{|\delta_{i+1}|} \right) \approx \alpha + \frac{4}{3\pi} \omega_\delta \delta_{mean,i} \quad (\text{Eq. 43})$$

Where:

$$\delta_{mean,i} = \frac{|\delta_i| + |\delta_{i+1}|}{2} \quad (\text{Eq. 44})$$

$$\omega_{\delta_0} = \sqrt{\omega_\delta^2 + \alpha_{eq}^2} \quad (\text{Eq. 45})$$

Considering both maxima and minima peaks, it is possible to evaluate  $\alpha_{eq}$  and  $\delta_{mean}$  for each cycle of the free decay simulation and then apply a linear regression fit on the evaluated points, with reference to equation (46). Using multiple points increases the accuracy of the evaluation of the linear and quadratic extinction according to equations (47) and (48).

$$\alpha_{eq} = a \cdot \delta_{mean} + b \quad (\text{Eq. 46})$$

$$\begin{cases} \alpha \equiv b \\ \beta \equiv \frac{3\pi}{4\omega_\delta} a \end{cases}$$

(Eqs. 47-48)

The linear regression results for the pitch and heave simulations are shown in figures (29) and (30), respectively, where the linear fit is shown together with the prediction interval. Table [10] reports the corresponding values of  $\alpha$  and  $\beta$ , together with the  $R^2$  value. In order for the results to be completely reliable, the  $R^2$  value should be higher than 0.8. However, this threshold has been reached only by the pitch free decay simulation. Even though the  $R^2$  value associated to the heave free decay results is not far from 0.8, it confirms that this motion is more critical and that an exhaustive investigation would be required to improve the quality of the results. Figures (29) and (30) show that all data points fall within the 95% range for both simulations, so both sets of estimated damping coefficients are considered valid and they are reported in table [10], as well. The calculation of these coefficients is based on the moments of inertia and on the added masses evaluated through the BEM software OrcaWave [95]. Finally, table [10] also reports the estimated natural frequencies of the platform for the two DOFs.

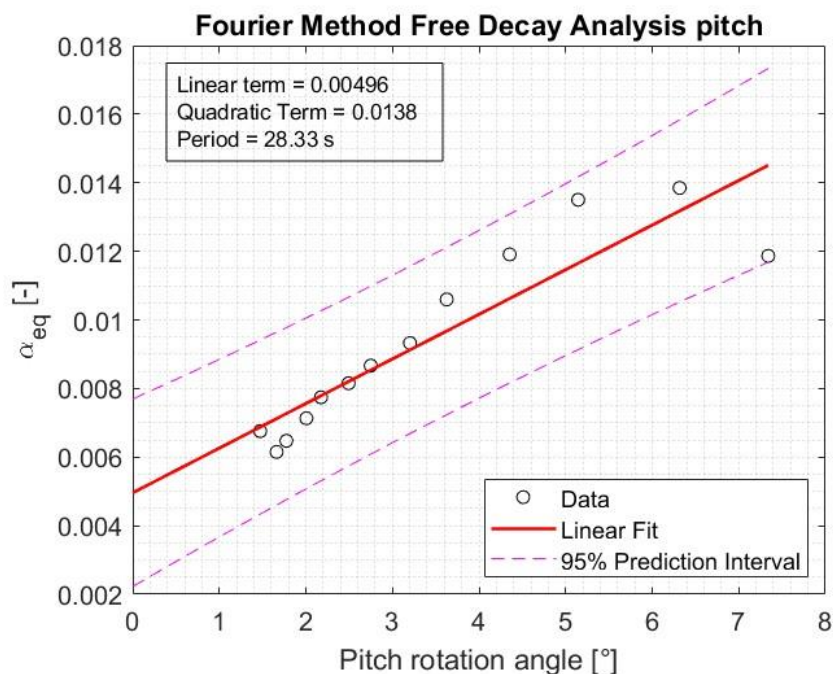


Figure 29 - Pitch data and outcomes from the linear regression fit.

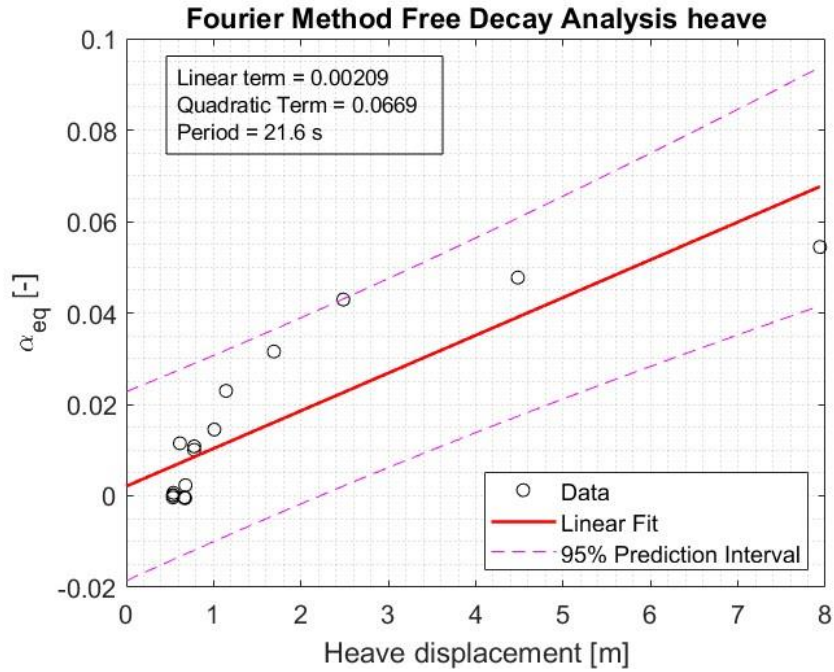


Figure 30 - Heave data and outcomes from the linear regression fit.

Table 10 - Results related to the hydrodynamic damping coefficients estimation for pitch and heave motions.

DOF	$\alpha$	$\beta$	$R^2$	$I$ [ $t^*m^2$ ], [t]	$A$ [ $t^*m^2$ ], [t]	$B_1$ [ $kN.m/(rad/s)$ ], [ $kN/(m/s)$ ]	$B_2$ [ $kN.m/(rad/s)^2$ ], [ $kN/(m/s)^2$ ]	Natural frequency (Hz)
Pitch (55)	0.0050	0.0138	0.81	4.45E+07	1.25E+07	5.65E+05	7.88E+05	0.035
Heave (33)	0.0021	0.0669	0.72	2.01E+04	2.74E+04	1.99E+02	3.18E+03	0.046

Unfortunately, no experimental data were available at the time this work has been written to correctly validate the results. Future tests on a scaled version of the platform are currently planned. Nonetheless, an attempt at comparing this work's results to previous studies has been done, thanks to the results reported by IEA in [14]. In the technical report, the platform's total hydrodynamic damping is represented in OpenFAST by adding results from a quadratic damping model, in the form of a viscous damping matrix for all DOFs, to HydroDyn's linear radiation damping model. The viscous damping model is obtained from SimpleFOAM simulations. Linear coefficients are not reported, while the pitch and heave components of the matrix are equal to  $1.676e10 [N \cdot s^2]$  and  $2.296e6 [N \cdot s^2/m^2]$ , respectively. The difference between the results is remarkable: the heave quadratic damping coefficient obtained in this work is almost 40% bigger than the reference value, while the pitch quadratic damping coefficient is around 2 orders of magnitude smaller. The comparison between the rigid-body natural frequencies is more promising: the evaluated pitch and heave natural frequencies are 2.7% and 6.1% smaller than the

corresponding values in IEA's report, respectively. As highlighted in the literature review, no validation process is reported for IEA's publication. Even though different works on the platform state that their numerical models' predictions compare well with experimental data on scaled versions of the FOWT, no data for the damping coefficients nor the natural frequencies are reported, making an accurate comparison impossible. Ongoing tests seem to confirm that the published results for VoltturnUS-S platform are questionable in terms of quadratic damping coefficients, but they are not ready yet and therefore they will not be taken as relevant sources to comment the present results. However, a single contradictory source is not considered enough to invalidate the results obtained in this work. In fact, the large difference between the results should represent an incentive to further investigate the theoretical foundations of the two evaluation methods employed, in order to identify eventual flaws and determine which one is more reliable. At the same time, further experimentation on the system, both scaled and full-scale, and open access to the corresponding data are needed to allow for the most accurate comparison. For these reasons, the coefficients obtained in this work will be confidently used in the next chapter to test their effect on the turbine productivity estimation.

## Case study productivity estimation

The final objective of this work is to use the damping coefficients obtained in the previous chapter to improve the performance of a lower-fidelity model. In particular, this chapter revolves around the simulation of the entire FOWT, i.e. the platform together with the 15MW turbine and the mooring lines, in OrcaFLEX in order to estimate the turbine's productivity over a year at a selected site and to compare the results obtained with and without the addition of damping coefficients.. Thanks to the collaboration with MORE Lab, the simulation template was already set up, including the platform model, mooring lines, wind and waves models.

A location offshore Lampedusa island, in Italy, has been selected as it is a well-known site for offshore energy production tests. The site is characterized by a good availability of wind resource, so that the use of such a big turbine can be justified. Nonetheless, results will be primarily judged qualitatively, rather than quantitatively. So, it is more relevant how the inclusion of damping coefficients affects the productivity estimation, than the produced energy itself.

In this chapter, the principle behind the dataset creation and processing will be explained first, in order to define the most significant environmental conditions to represent a typical year. Then, the results from simulations with and without damping coefficients will be reported and compared in terms of power profile, estimated productivity, and capacity factor. Unfortunately, a techno-economic evaluation could not be performed in this thesis because both the semi-submersible platform and the turbine are not commercially available, and so any estimation on capital and operational expenditures would not be an accurate enough to produce a reliable evaluation.

### Environmental conditions selection

Local wind and wave resource data have been taken from ERA5 database from the European Center for Medium-range Weather Forecasts (ECMWF) web page [96]. The dataset contains tri-hour data in the region of interest over the last 60 years, for a total of 172400 registered events. In particular, each event is described by the wind speed at 100m height, the significant height of combined wind waves and swell, and the peak wave period. The dataset has been cleaned, removing invalid or missing data points, leaving just over 149000 valid entries. Then, the events have been sorted in bins, according to the limits in table [11]. Wind speed intervals are based on IEA's technical report data defining the 15MW reference wind turbine

[15], so that all wind speeds below the cut-in speed of 3 m/s are grouped together and the same is done for wind speeds above the cut-out speed of 25 m/s. Between these two values, events have been divided in eight equally spaced groups. Eight wave significant height intervals and six peak period intervals are arbitrarily created to include the maximum values registered at the selected location. Then, twenty bins have been selected as the most significant ones, as they overall cover around 90% of the events in a year. Therefore, they represent the most probable environmental conditions in which the turbine would be operating. In fact, the number of intervals for each descriptor of the environmental conditions has been kept low enough to limit the amount of bins necessary to describe the large majority of events in a typical year. Table [12] reports the twenty selected bins in descending order of percentage of occurrence: each group is described by the percentage of events covered for a typical year and by the average values of each descriptor, evaluated as the arithmetic mean between the descriptors of the events included in that bin.

Table 11 - Values delimiting the bins for each environmental conditions descriptor.

<b>Wind speed [m/s]</b>	0.00	3.00	5.75	8.50	11.25	14.00	16.75	19.50	22.25	25.00	28.00
<b>Wave significant height [m]</b>	0.00	1.00	2.00	3.00	4.00	5.00	6.00	7.00	8.00		
<b>Wave peak period [s]</b>	0.00	2.00	4.00	6.00	8.00	12.00	14.00				

Table 12 - 20 significant environmental conditions sets for the turbine's productivity estimation.

<b>Bin</b>	<b>Occurrence [%]</b>	<b>V<sub>ave</sub> [m/s]</b>	<b>H<sub>save</sub> [m]</b>	<b>T<sub>pave</sub> [s]</b>
1	12.27	4.4	0.57	4.91
2	10.59	6.98	0.76	4.83
3	7.47	9.86	1.27	5.31
4	6.96	1.94	0.45	4.88
5	5.65	4.38	0.35	3.34
6	4.89	9.86	1.57	6.57
7	4.53	6.97	0.54	3.49
8	4.24	4.32	0.7	6.51
9	3.74	12.35	1.46	5.37
10	3.73	1.9	0.25	3.43
11	3.66	7.26	1.32	6.7
12	3.22	9.47	0.85	4.63
13	3.08	7.56	1.13	5.46
14	2.79	12.8	2.27	7.05
15	2.74	1.94	0.61	6.49
16	2.37	12.25	1.78	6.41
17	2.19	15.11	2.51	7.01
18	1.79	6.78	0.8	6.57
19	1.53	4.66	1.23	6.83
20	1.2	9.47	0.69	3.66

## Productivity estimation and comparison

In order to estimate the turbine productivity, the FOWT behavior is simulated for each of the selected environmental conditions in table [12]. In particular, the wind distribution is related to the Norwegian Petroleum Directorate (NPD) spectrum as reported in OrcaFlex user manual [20], [97], while waves are linked to the Joint North Sea Wave Project (JONSWAP) spectrum [98], with a  $\gamma$  parameter equal to 3.3 and a frontal incoming wave. For each condition, the turbine behavior has been separately simulated with and without the inclusion of damping coefficients for the pitch and heave DOFs. Each simulation is run with an initial transient period of 500s, followed by a 3600s period from which the produced power values are extrapolated. Then, the average power is evaluated together with the standard deviation, and the results are reported in table [13]. It is immediately clear that the average power values are almost unaffected by the inclusion of damping coefficients, suggesting that they are not compulsory for the productivity estimation. The motion of the platform is, however, different between the two cases, as a discrete Fourier analysis revealed (the results of which are not reported for simplicity) and as remarked by the values of the standard deviation. As the standard deviation of the produced power profile is generally lower when damping coefficients are used, it can be assumed that the platform is more stable, with the additional benefit of a less variable power injection in the grid. It is important to notice that, even if damping coefficients do not have an effect on the productivity estimation, they would still be useful for the investigation of other quantities like structural loads and moorings' lifetime, which could be the object of future studies on this topic. As the greatest difference for the standard deviation can be seen for the 14<sup>th</sup> bin, for which it is reduced by more than 9%, figure (31) shows a detail of the power profile estimated in the corresponding environmental conditions, from 1000s to 2000s. The figure highlights how the average power is similar in the two cases, but that when the damping coefficients are used it oscillates slightly less.

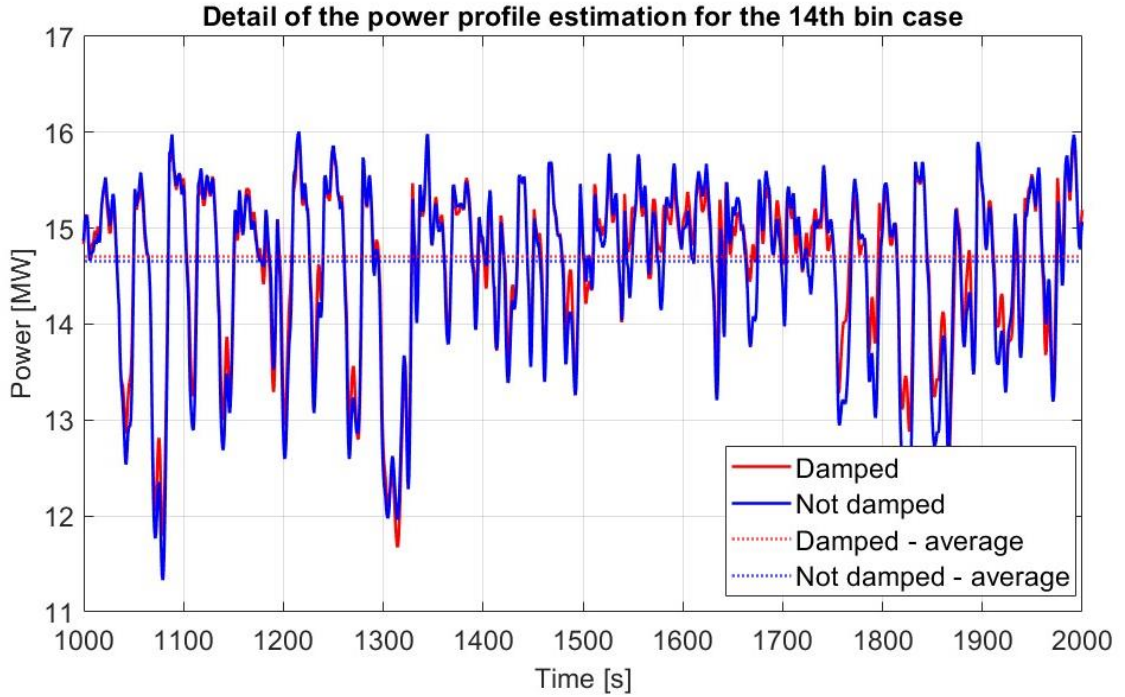


Figure 31 - Comparison of the estimated power profile in the environmental conditions of the 14<sup>th</sup> bin, from 1000s to 2000s.

Table 13 – Average power, standard deviation of the power profile and energy produced for each relevant bin of environmental conditions.

Bin	P <sub>ave</sub> [MW]		P <sub>std</sub> [kW]		E [MWh]	
	Damping	No Damping	Damping	No Damping	Damping	No Damping
1	1.58	1.58	187.44	187.97	1700.66	1700.70
2	7.05	7.05	714.49	717.79	6537.85	6537.96
3	12.01	12.00	932.50	949.22	7857.29	7848.48
4	0.00	0.00	0.00	0.00	0.00	0.00
5	1.56	1.56	184.68	185.20	769.90	769.92
6	12.01	12.00	936.63	951.66	5149.29	5143.93
7	7.02	7.02	711.79	715.09	2784.42	2784.46
8	1.48	1.48	175.92	176.41	549.48	549.48
9	14.60	14.56	772.60	824.29	4783.95	4772.06
10	0.00	0.00	0.00	0.00	0.00	0.00
11	7.90	7.90	783.53	787.20	2530.29	2530.32
12	11.42	11.40	891.03	911.28	3220.08	3215.96
13	8.82	8.82	787.07	792.46	2376.58	2376.65
14	14.71	14.66	732.95	807.09	3596.12	3584.34
15	0.00	0.00	0.00	0.00	0.00	0.00
16	14.57	14.53	790.43	840.56	3022.12	3014.71
17	14.89	14.87	649.94	701.23	2863.10	2859.17
18	6.47	6.47	653.90	656.94	1013.10	1013.11
19	1.95	1.95	224.84	225.48	260.42	260.43
20	11.42	11.40	891.51	911.91	1198.23	1196.66

From the average values of power of each bin, the produced energy is evaluated from equation (49), where  $p_i \cdot 365 \cdot 24$  are the hours in a year during which the turbine is producing the average power obtained for bin  $i$ , as  $p_i$  is the occurrence of the bin as a percentage value. Assuming that the contribution of the bins that were not part of the productivity estimation is negligible, the annual energy production is simply obtained by summing the energy estimated for each simulated bin. As anticipated, the use of the damping coefficients does not significantly change the estimated productivity: the annual energy production is equal to  $5.02e4 MWh$  when the coefficients are used, and to  $5.01e4 MWh$  when they are ignored. From the annual energy production, it is possible to estimate the Capacity Factor (CF) through equation (50), where  $E_{ref}$  is the amount of energy produced by the turbine if it was able to continuously generate its rated power.

$$E_i = p_i \cdot 365 \frac{d}{y} \cdot 24 \frac{h}{d} \cdot P_{ave,i} \quad (\text{Eq. 49})$$

$$CF = \frac{\sum_{i=1}^{20} E_i}{E_{ref}} \quad (\text{Eq. 50})$$

The CF is equal to 38.21% when the damping coefficients are used in the simulations, and to 38.17% when they are not used. It is interesting to notice that this result is aligned to the average CF of offshore wind farms estimated by Wind Europe in its 2022 report, which is equal to 36% [99]. Even though the CF is expected to change if a wind farm is simulated instead of an isolated turbine, the results of this thesis are promising enough to encourage future studies focusing on the possibility to deploy IEA's 15MW turbine at the selected location. These studies could focus on more accurate modelling of the turbine's behavior, on the techno-economic performance of an hypothetical wind farm, as well as on the performance of the FOWT in other areas of the Mediterranean region.

## Conclusion

This thesis focused on the investigation of the effect of accurate damping coefficients obtained from high-fidelity simulations on the productivity estimation through the lower-fidelity software OrcaFlex. Focusing on UMaine's VoltturnUS-S platform, CFD simulations of the pitch and heave free decay motions of the platform have been performed. Convergence studies on the space and time discretization parameters have been run, proving that the asymptotic range was reached in all cases. Accurate tests revealed that the included models contributed to reaching a good compromise between the accuracy of the results and the minimization of the computational time. The DFBI model, in particular, was responsible for a large increase of the computational time, that was reduced by limiting the maximum number of iterations allowed for its corresponding 6-DOF solver when simulating pitch motion. However, the same result could not be obtained for the heave free decay simulation, as this work revealed that a more in-depth investigation is required to improve the corresponding simulation setup. In particular, it is suggested to focus future works on the optimization of the performance of the overset grid technique and of the mesh refinement. At the same time, it would be beneficial to test alternative models, e.g. the possibility to solve the platform motion by coupling Star-CCM+ to MATLAB's Simulink is currently under study [100].

The results of the free decay tests have then been used to extrapolate linear and non-linear damping coefficients, as well as natural frequencies, through a linear regression fit technique, which confirmed the need to improve the quality of heave free decay results. This chapter also highlighted the urgent need of experimental tests to validate the numerical results and, more importantly, the coefficient estimation technique. In fact, no valid data have been found in the literature that could definitively assess the reliability of the results.

Finally, simulations under environmental conditions from real world data revealed that the use of accurate damping coefficients does not affect the productivity estimation for the turbine, but it has an impact on the stability of the platform, and thus on the variability of the energy injection in the electricity grid. Nonetheless, the estimated energy production and CF are promising when compared to the performance of existing systems. An accurate investigation of the results showed a difference in the platform motions, that could translate in a more accurate estimation of other relevant quantities. In particular, future works could explore other paths like the estimation of damping coefficients for the remaining DOFs, the inclusion of mooring lines in the CFD simulations, and the investigation of the structural loads.

## Bibliography

- [1] IEA, “Renewables 2022 - Analysis and forecast to 2027,” Jan. 2023.
- [2] U. von der Leyen, “2023 State of the Union Address by President von der Leyen.” Accessed: Sep. 14, 2023. [Online]. Available: [https://ec.europa.eu/commission/presscorner/detail/en/speech\\_23\\_4426](https://ec.europa.eu/commission/presscorner/detail/en/speech_23_4426)
- [3] IEA, “Offshore Wind Outlook 2019,” Nov. 2019.
- [4] IRENA and GWEC, “Enabling frameworks for offshore wind scaleup: Innovations in permitting,” Abu Dhabi, 2023.
- [5] C. L. Archer and M. Jacobson, “Evaluation of global wind power,” *J Geophys Res*, vol. 110, 2005, doi: 10.1029/2004JD005462.
- [6] S. Butterfield, W. Musical, J. Jonkman, P. Sclavounos, and L. Wayman, “Engineering Challenges for Floating Offshore Wind Turbines,” in *Copenhagen Offshore Wind International Conference and Expedition (COW05)*, Copenhagen, Denmark, Oct. 2005.
- [7] Y. Bae, M. Kim, Q. Yu, and K. Kim, “Influence of control strategy to FOWT hull motions by aero-elastic-control-floater-mooring coupled analysis,” in *International Offshore & Polar Engineering Conference*, International Society of Offshore and Polar Engineers, 2011.
- [8] E. C. Edwards, A. Holcombe, S. Brown, E. Ransley, M. Hann, and D. Greaves, “Evolution of floating offshore wind platforms: A review of at-sea devices,” *Renewable and Sustainable Energy Reviews*, vol. 183, Sep. 2023, doi: 10.1016/j.rser.2023.113416.
- [9] B. Skaare, F. G. Nielsen, T. D. Hanson, R. Yttervik, O. Havmøller, and A. Rekdal, “Analysis of measurements and simulations from the Hywind Demo floating wind turbine,” *Wind Energy*, vol. 18, no. 6, pp. 1105–1122, Jun. 2015, doi: 10.1002/we.1750.
- [10] BBC, “Floating wind farm to be installed off Peterhead.” Accessed: Jul. 01, 2023. [Online]. Available: <https://www.bbc.com/news/uk-scotland-scotland-business-34694463>
- [11] J. Jonkman and W. Musial, “Offshore Code Comparison Collaboration (OC3) for IEA Task 23 Offshore Wind Technology and Deployment,” Dec. 2010.
- [12] A. Robertson *et al.*, “Definition of the Semisubmersible Floating System for Phase II of OC4,” Sep. 2014.
- [13] A. N. Robertson *et al.*, “OC5 Project Phase II: Validation of Global Loads of the DeepCwind Floating Semisubmersible Wind Turbine,” *Energy Procedia*, vol. 137, pp. 38–57, Oct. 2017, doi: 10.1016/j.egypro.2017.10.333.

- [14] C. Allen *et al.*, “Definition of the UMaine VoltturnUS-S Reference Platform Developed for the IEA Wind 15-Megawatt Offshore Reference Wind Turbine,” Golden, CO (United States), Jul. 2020. doi: 10.2172/1660012.
- [15] E. Gaertner *et al.*, “IEA Wind TCP Task 37: Definition of the IEA 15-Megawatt Offshore Reference Wind Turbine,” Golden, CO (United States), Mar. 2020. doi: 10.2172/1603478.
- [16] T. T. Tran and D.-H. Kim, “A CFD study of coupled aerodynamic-hydrodynamic loads on a semisubmersible floating offshore wind turbine,” *Wind Energy*, vol. 21, no. 1, pp. 70–85, Jan. 2018, doi: 10.1002/we.2145.
- [17] F. Lemmer, K. Müller, W. Yu, R. Faerron Guzman, and M. Kretschmer, “LIFES50+ project - Deliverable D4.3 Optimization framework and methodology for optimized floater design,” 2016.
- [18] A. M. Viselli, A. J. Goupee, H. J. Dagher, and C. K. Allen, “VoltturnUS 1:8: Conclusion of 18-Months of Operation of the First Grid-Connected Floating Wind Turbine Prototype in the Americas,” in *Volume 9: Ocean Renewable Energy*, American Society of Mechanical Engineers, May 2015. doi: 10.1115/OMAE2015-41065.
- [19] A. M. Viselli, A. J. Goupee, and H. J. Dagher, “Model Test of a 1:8-Scale Floating Wind Turbine Offshore in the Gulf of Maine,” *Journal of Offshore Mechanics and Arctic Engineering*, vol. 137, no. 4, Aug. 2015, doi: 10.1115/1.4030381.
- [20] Orcina Ltd., “OrcaFlex Help.” Accessed: Aug. 29, 2023. [Online]. Available: <https://www.orcina.com/webhelp/OrcaFlex/Default.htm>
- [21] CD-Adapco, “STAR CCM+ User Guide Version 12.04,” *CD-Adapco*. New York, NY, USA, 2017.
- [22] N. Luo, L. Pacheco, Y. Vidal, and H. Li, “Dynamic load mitigation for floating offshore wind turbines supported by structures with mooring lines,” in *Proceedings of the 5th European Conference on Structural Control*, Genoa, Italy, Jun. 2012, pp. 48–56.
- [23] T. T. Tran and D.-H. Kim, “Fully coupled aero-hydrodynamic analysis of a semi-submersible FOWT using a dynamic fluid body interaction approach,” *Renew Energy*, vol. 92, pp. 244–261, Jul. 2016, doi: 10.1016/j.renene.2016.02.021.
- [24] ANSYS Inc., *AQWA Reference Manual*, 14.5. Canonsbourg, PA 15317, 2012.
- [25] WAMIT Inc., *WAMIT® User Manual Version 7.4*. Chestnut Hill, MA, USA, 2020.
- [26] National Renewable Energy Laboratory, “OpenFAST Documentation.” Accessed: Aug. 29, 2023. [Online]. Available: <https://openfast.readthedocs.io/en/main/index.html>
- [27] National Renewable Energy Laboratory, “HydroDyn User Guide and Theory Manual.” Accessed: Aug. 29, 2023. [Online]. Available: <https://openfast.readthedocs.io/en/main/source/user/hydrodyn/index.html>

- [28] OpenCFD Ltd, “User Guide.” Accessed: Sep. 01, 2023. [Online]. Available: <https://www.openfoam.com/documentation/user-guide>
- [29] H. Glauert, “Airplane Propellers,” in *Aerodynamic theory*, New York, 1963.
- [30] S. G. Voutsinas, M. A. Belessis, and K. G. Rados, “Investigation of the yawed operation of wind turbines by means of a vortex particle method,” in *Agard Conference Proceedings*, Neuilly sur Seine, France: AGARD, 1995, pp. 11.1-11.11.
- [31] G. J. W. Van Bussel, “The aerodynamics of horizontal axis wind turbine rotors explored with asymptotic expansion methods,” Thesis/dissertation, Technische Universiteit Delft, Delft (Netherlands), 1995.
- [32] J. N. Sørensen and W. Z. Shen, “Numerical Modeling of Wind Turbine Wakes,” *J Fluids Eng*, vol. 124, no. 2, pp. 393–399, Jun. 2002, doi: 10.1115/1.1471361.
- [33] H. Zhou and D. Wan, “Numerical investigations on the aerodynamic performance of wind turbine: Downwind versus upwind configuration,” *Journal of Marine Science and Application*, vol. 14, no. 1, pp. 61–68, Mar. 2015, doi: 10.1007/s11804-015-1295-9.
- [34] J. M. Jonkman, “Dynamics of offshore floating wind turbines-model development and verification,” *Wind Energy*, vol. 12, no. 5, pp. 459–492, Jul. 2009, doi: 10.1002/we.347.
- [35] T. T. Tran and D. H. Kim, “The aerodynamic interference effects of a floating offshore wind turbine experiencing platform pitching and yawing motions,” *Journal of Mechanical Science and Technology*, vol. 29, no. 2, pp. 549–561, Feb. 2015, doi: 10.1007/s12206-015-0115-0.
- [36] T. T. Tran and D.-H. Kim, “A CFD study into the influence of unsteady aerodynamic interference on wind turbine surge motion,” *Renew Energy*, vol. 90, pp. 204–228, May 2016, doi: 10.1016/j.renene.2015.12.013.
- [37] T. Toan Tran, D.-H. Kim, and B. Hieu Nguyen, “Aerodynamic Interference Effect of Huge Wind Turbine Blades With Periodic Surge Motions Using Overset Grid-Based Computational Fluid Dynamics Approach,” *J Sol Energy Eng*, vol. 137, no. 6, Dec. 2015, doi: 10.1115/1.4031184.
- [38] M. Masciola, J. Jonkman, and A. Robertson, “Extending the Capabilities of the Mooring Analysis Program: A Survey of Dynamic Mooring Line Theories for Integration Into FAST,” in *Proceedings of the ASME 2014 33rd International Conference on Ocean, Offshore and Arctic Engineering. Volume 9A: Ocean Renewable Energy*, San Francisco, California, USA: American Society of Mechanical Engineers, Jun. 2014. doi: 10.1115/OMAE2014-23508.
- [39] M. Hall, “MoorDyn User’s Guide.” Accessed: Sep. 12, 2023. [Online]. Available: <http://www.matt-hall.ca/files/MoorDyn%20Users%20Guide%202015-12-15.pdf>

- [40] H. Huang and H.-C. Chen, “Investigation of mooring damping effects on vortex-induced motion of a deep draft semi-submersible by coupled CFD-FEM analysis,” *Ocean Engineering*, vol. 210, p. 107418, Aug. 2020, doi: 10.1016/j.oceaneng.2020.107418.
- [41] Y. Liu, Q. Xiao, A. Incecik, C. Peyrard, and D. Wan, “Establishing a fully coupled CFD analysis tool for floating offshore wind turbines,” *Renew Energy*, vol. 112, pp. 280–301, Nov. 2017, doi: 10.1016/j.renene.2017.04.052.
- [42] Maritime Research Institute Netherlands (MARIN), “ANYSIM XMF.” Accessed: Sep. 02, 2023. [Online]. Available: <https://www.marin.nl/en/about/facilities-and-tools/software/ansysim>
- [43] A. J. Dunbar, B. A. Craven, and E. G. Paterson, “Development and validation of a tightly coupled CFD/6-DOF solver for simulating floating offshore wind turbine platforms,” *Ocean Engineering*, vol. 110, pp. 98–105, Dec. 2015, doi: 10.1016/J.OCEANENG.2015.08.066.
- [44] T. T. Tran and D.-H. Kim, “The coupled dynamic response computation for a semi-submersible platform of floating offshore wind turbine,” *Journal of Wind Engineering and Industrial Aerodynamics*, vol. 147, pp. 104–119, Dec. 2015, doi: 10.1016/j.jweia.2015.09.016.
- [45] C. W. Hirt and B. D. Nichols, “Volume of fluid (VOF) method for the dynamics of free boundaries,” *J Comput Phys*, vol. 39, no. 1, pp. 201–225, Jan. 1981, doi: 10.1016/0021-9991(81)90145-5.
- [46] F. R. Menter, “Improved two-equation k-omega turbulence models for aerodynamic flows,” Document ID: 19930013620, Oct. 1992.
- [47] P. Spalart and S. Allmaras, “A one-equation turbulence model for aerodynamic flows,” in *30th Aerospace Sciences Meeting and Exhibit*, Reston, Virginia: American Institute of Aeronautics and Astronautics, Jan. 1992. doi: 10.2514/6.1992-439.
- [48] B. E. Launder and B. I. Sharma, “Application of the energy-dissipation model of turbulence to the calculation of flow near a spinning disc,” *Letters in Heat and Mass Transfer*, vol. 1, no. 2, pp. 131–137, Nov. 1974, doi: 10.1016/0094-4548(74)90150-7.
- [49] OpenCFD Ltd., “OpenFOAM v2306.” 2023.
- [50] M. A. Benitz, D. P. Schmidt, M. A. Lackner, G. M. Stewart, J. Jonkman, and A. Robertson, “Comparison of Hydrodynamic Load Predictions Between Engineering Models and Computational Fluid Dynamics for the OC4-DeepCwind Semi-Submersible: Preprint,” in *Conference: Presented at the ASME 2014 33rd International Conference on Ocean, Offshore and Arctic Engineering (OMAE2014)*, San Francisco, California, USA: American Society of Mechanical Engineers, Jun. 2014. doi: 10.1115/OMAE2014-23985.

- [51] P. Cheng, Y. Huang, and D. Wan, “A numerical model for fully coupled aero-hydrodynamic analysis of floating offshore wind turbine,” *Ocean Engineering*, vol. 173, pp. 183–196, Feb. 2019, doi: 10.1016/j.oceaneng.2018.12.021.
- [52] Y. Wang, H.-C. Chen, G. Vaz, and S. Burmester, “CFD Simulation of Semi-Submersible Floating Offshore Wind Turbine Under Pitch Decay Motion,” in *ASME 2019 2nd International Offshore Wind Technical Conference*, American Society of Mechanical Engineers, Nov. 2019. doi: 10.1115/IOWTC2019-7515.
- [53] S. Burmester, G. Vaz, S. Gueydon, and O. el Moctar, “Investigation of a semi-submersible floating wind turbine in surge decay using CFD,” *Ship Technology Research*, vol. 67, no. 1, pp. 2–14, Jan. 2020, doi: 10.1080/09377255.2018.1555987.
- [54] G. Vaz, F. Jaouen, and M. Hoekstra, “Free-Surface Viscous Flow Computations: Validation of URANS Code FreSCo,” in *Volume 5: Polar and Arctic Sciences and Technology; CFD and VIV*, ASMEDC, Jan. 2009, pp. 425–437. doi: 10.1115/OMAE2009-79398.
- [55] A. de Boer, M. S. van der Schoot, and H. Bijl, “Mesh deformation based on radial basis function interpolation,” *Comput Struct*, vol. 85, no. 11–14, pp. 784–795, Jun. 2007, doi: 10.1016/j.compstruc.2007.01.013.
- [56] F. Menter, M. Kuntz, and R. B. Langtry, “Ten years of industrial experience with the SST turbulence model,” *Heat and Mass Transfer*, vol. 4, Aug. 2003.
- [57] C. M. Klaij, M. Hoekstra, and G. Vaz, “Design, analysis and verification of a volume-of-fluid model with interface-capturing scheme,” *Comput Fluids*, vol. 170, pp. 324–340, Jul. 2018, doi: 10.1016/j.compfluid.2018.05.016.
- [58] C. J. Greenshields, “OpenFoam: Open Source CFD: Documentation.” Accessed: Aug. 19, 2023. [Online]. Available: <https://www.openfoam.com/documentation/>
- [59] A. M. Viselli, A. J. Goupee, H. J. Dagher, and C. K. Allen, “Design and model confirmation of the intermediate scale VoltturnUS floating wind turbine subjected to its extreme design conditions offshore Maine,” *Wind Energy*, vol. 19, no. 6, pp. 1161–1177, Jun. 2016, doi: 10.1002/we.1886.
- [60] C. Allen, A. Goupee, H. Dagher, and A. Viselli, “Validation of Global Performance Numerical Design Tools Used for Design of Floating Offshore Wind Turbines,” in *Proceedings of the ASME 2015 34th International Conference on Ocean, Offshore and Arctic Engineering. Volume 9: Ocean Renewable Energy*, St. John’s, Newfoundland, Canada, Jun. 2015. doi: 10.1115/OMAE2015-41437.
- [61] M. Philippe, A. Babarit, and P. Ferrant, “Aero-Hydro-Elastic Simulation of a Semi-Submersible Floating Wind Turbine,” *Journal of Offshore Mechanics and Arctic Engineering*, vol. 136, no. 2, May 2014, doi: 10.1115/1.4025031.

- [62] F. Beyer, M. Arnold, and P. W. Cheng, “Analysis of Floating Offshore Wind Turbine Hydrodynamics Using coupled CFD and Multibody Methods,” in *Proceedings of the Twenty-third (2013) International Offshore and Polar Engineering*, Anchorage, Alaska, USA, Jun. 2013, pp. 261–267.
- [63] ANSYS Inc., “ANSYS CFX.” Accessed: Aug. 29, 2023. [Online]. Available: <https://www.ansys.com/it-it/products/fluids/ansys-cfx>
- [64] Dassault Systèmes, “SIMPACK.” Accessed: Aug. 29, 2023. [Online]. Available: <https://www.3ds.com/products-services/simulia/products/simpack/>
- [65] S. Quallen, T. Xing, P. Carrica, Y. Li, and J. Xu, “CFD Simulation of a Floating Offshore Wind Turbine System Using a Quasi-static Crowfoot Mooring-Line Model,” *Journal of Ocean and Wind Energy*, vol. 1, pp. 143–152, Aug. 2014.
- [66] The University of Iowa, “CFDSHIP-Iowa.” Accessed: Aug. 29, 2023. [Online]. Available: <https://www2.ihr.uiowa.edu/shiphydro/cfd-code/>
- [67] P. M. Carrica, R. V. Wilson, R. W. Noack, and F. Stern, “Ship motions using single-phase level set with dynamic overset grids,” *Comput Fluids*, vol. 36, no. 9, pp. 1415–1433, Nov. 2007, doi: 10.1016/j.compfluid.2007.01.007.
- [68] P. J. Roache, *Verification and Validation in Computational Science and Engineering*. Albuquerque, New Mexico, USA: hermosa publishers, 1998.
- [69] Y. Wang, H.-C. Chen, A. Koop, and G. Vaz, “Hydrodynamic response of a FOWT semi-submersible under regular waves using CFD: Verification and validation,” *Ocean Engineering*, vol. 258, p. 111742, Aug. 2022, doi: 10.1016/j.oceaneng.2022.111742.
- [70] H. W. Coleman and F. Stern, “Uncertainties and CFD Code Validation,” *J Fluids Eng*, vol. 119, no. 4, pp. 795–803, Dec. 1997, doi: 10.1115/1.2819500.
- [71] A. Robertson, E. E. Bachynski, S. Gueydon, F. Wendt, and P. Schünemann, “Total experimental uncertainty in hydrodynamic testing of a semisubmersible wind turbine, considering numerical propagation of systematic uncertainty,” *Ocean Engineering*, vol. 195, p. 106605, Jan. 2020, doi: 10.1016/j.oceaneng.2019.106605.
- [72] P. J. Roache, “Perspective: A Method for Uniform Reporting of Grid Refinement Studies,” *J Fluids Eng*, vol. 116, no. 3, pp. 405–413, Sep. 1994, doi: 10.1115/1.2910291.
- [73] L. Eça and M. Hoekstra, “A procedure for the estimation of the numerical uncertainty of CFD calculations based on grid refinement studies,” *J Comput Phys*, vol. 262, pp. 104–130, Apr. 2014, doi: 10.1016/J.JCP.2014.01.006.
- [74] T. Tran, D. Kim, and J. Song, “Computational Fluid Dynamic Analysis of a Floating Offshore Wind Turbine Experiencing Platform Pitching Motion,” *Energies (Basel)*, vol. 7, no. 8, pp. 5011–5026, Aug. 2014, doi: 10.3390/en7085011.

- [75] A. J. Coulling, A. J. Goupee, A. N. Robertson, J. M. Jonkman, and H. J. Dagher, “Validation of a FAST semi-submersible floating wind turbine numerical model with DeepCwind test data,” *Journal of Renewable and Sustainable Energy*, vol. 5, no. 2, Mar. 2013, doi: 10.1063/1.4796197.
- [76] C. Luan, Z. Gao, and T. Moan, “Modelling and Analysis of a Semi-Submersible Wind Turbine With a Central Tower With Emphasis on the Brace System,” in *Proceedings of the ASME 2013 32nd International Conference on Ocean, Offshore and Arctic Engineering. Volume 8: Ocean Renewable Energy*, Nantes, France: American Society of Mechanical Engineers, Jun. 2013. doi: 10.1115/OMAE2013-10408.
- [77] P.-Å. Krogstad and J. A. Lund, “An experimental and numerical study of the performance of a model turbine,” *Wind Energy*, vol. 15, no. 3, pp. 443–457, Apr. 2012, doi: 10.1002/we.482.
- [78] R. L. Meakin, “Composite overset structured grids,” in *Handbook of Grid Generation*, Boca Raton, FL, USA: CRC Press, 1999, pp. 1–20.
- [79] N. A. Petersson, “Hole-Cutting for Three-Dimensional Overlapping Grids,” *SIAM Journal on Scientific Computing*, vol. 21, no. 2, pp. 646–665, Jan. 1999, doi: 10.1137/S1064827597329102.
- [80] M. Fontana, P. Casalone, S. A. Sirigu, G. Giorgi, G. Bracco, and G. Mattiazzo, “Viscous Damping Identification for a Wave Energy Converter Using CFD-URANS Simulations,” *J Mar Sci Eng*, vol. 8, no. 5, p. 355, May 2020, doi: 10.3390/jmse8050355.
- [81] F. Menter, “Zonal Two Equation k-w Turbulence Models For Aerodynamic Flows,” in *Proceedings of the 23rd Fluid Dynamics, Plasmadynamics, and Lasers Conference*, Orlando, Florida, USA: American Institute of Aeronautics and Astronautics, Jul. 1993, p. 2906. doi: 10.2514/6.1993-2906.
- [82] F. R. Menter, “Two-equation eddy-viscosity turbulence models for engineering applications,” *AIAA Journal*, vol. 32, no. 8, pp. 1598–1605, Aug. 1994, doi: 10.2514/3.12149.
- [83] T. H. Shih, W. W. Liou, A. Shabbir, Z. Yang, and J. Zhu, “A new k-epsilon eddy viscosity model for high Reynolds number turbulent flows: Model development and validation,” Washington, DC, USA, Document ID: 19950005029, 1994.
- [84] S. Mayer and P. A. Madsen, “Simulation of Breaking Waves in the Surf Zone using a Navier-Stokes Solver,” in *Proceedings of the 25th International Conference of Coastal Engineering 2000*, Sidney, Australia: American Society of Civil Engineers, Mar. 2001, pp. 928–941. doi: 10.1061/40549(276)72.
- [85] B. E. Larsen and D. R. Fuhrman, “On the over-production of turbulence beneath surface waves in Reynolds-averaged Navier–Stokes models,” *J Fluid Mech*, vol. 853, pp. 419–460, Oct. 2018, doi: 10.1017/jfm.2018.577.

- [86] P. Casalone, O. Dell’edera, M. Fontana, B. Battisti, and G. Mattiazzo, “Solutions to Wave Damping Over Time in CFD RANS Simulations Due to Exponential Generation of Numerical Turbulence,” in *Proceedings of the International Conference on Offshore Mechanics and Arctic Engineering - OMAE*, Hamburg, Germany: American Society of Mechanical Engineers Digital Collection, Oct. 2022. doi: 10.1115/OMAE2022-81447.
- [87] M. S. Gritskevich, A. V. Garbaruk, J. Schütze, and F. R. Menter, “Development of DDES and IDDES Formulations for the  $k-\omega$  Shear Stress Transport Model,” *Flow Turbul Combust*, vol. 88, no. 3, pp. 431–449, Apr. 2012, doi: 10.1007/s10494-011-9378-4.
- [88] H. Reichardt, “Vollständige Darstellung der turbulenten Geschwindigkeitsverteilung in glatten Leitungen,” *ZAMM - Zeitschrift für Angewandte Mathematik und Mechanik*, vol. 31, no. 7, pp. 208–219, 1951, doi: 10.1002/zamm.19510310704.
- [89] I. Celik and O. Karatekin, “Numerical Experiments on Application of Richardson Extrapolation With Nonuniform Grids,” *J Fluids Eng*, vol. 119, no. 3, pp. 584–590, Sep. 1997, doi: 10.1115/1.2819284.
- [90] I. Celik, J. Li, G. Hu, and C. Shaffer, “Limitations of Richardson Extrapolation and Some Possible Remedies,” *J Fluids Eng*, vol. 127, no. 4, pp. 795–805, Jul. 2005, doi: 10.1115/1.1949646.
- [91] The MathWorks Inc., “MATLAB documentation.” Accessed: Sep. 01, 2023. [Online]. Available: <https://it.mathworks.com/help/matlab/index.html?lang=en>
- [92] G. H. Keulegan and L. H. Carpenter, “Forces on cylinders and plates in an oscillating fluid,” *J Res Natl Bur Stand (1934)*, vol. 60, no. 5, p. 423, May 1958, doi: 10.6028/jres.060.043.
- [93] F. Balduzzi, A. Bianchini, G. Ferrara, and L. Ferrari, “Dimensionless numbers for the assessment of mesh and timestep requirements in CFD simulations of Darrieus wind turbines,” *Energy*, vol. 97, pp. 246–261, Feb. 2016, doi: 10.1016/j.energy.2015.12.111.
- [94] W. Cummins, “The Impulse Response Function and Ship Motions,” Washington, DC, USA, Oct. 1962.
- [95] Orcina Ltd., “OrcaWave Guide.” Accessed: Aug. 01, 2023. [Online]. Available: Orcina Ltd.
- [96] European Center for Medium-range Weather Forecasts (ECMWF), “ERA5 hourly data on single levels from 1940 to present.” Accessed: Jul. 01, 2023. [Online]. Available: <https://cds.climate.copernicus.eu/cdsapp#!/dataset/reanalysis-era5-single-levels?tab=form>
- [97] NPD, “Regulations relating to loadbearing structures in the petroleum activities,” 1995.
- [98] K. Hasselmann *et al.*, “Measurements of wind-wave growth and swell decay during the joint North Sea wave project (JONSWAP),” *Ergänzungsheft zur Deutschen Hydrographischen Zeitschrift, Reihe A*, vol. 12, 1973.

- [99] WindEurope, "Wind energy in Europe - 2022 statistics and the outlook for 2023-2027," Feb. 2023.
- [100] The MathWorks Inc., "Simulink Documentation." Accessed: Sep. 01, 2023. [Online]. Available: <https://it.mathworks.com/help/simulink/index.html?lang=en>